

Primordial Black Holes from First-Order Phase Transition in the xSM

Dorival Gonçalves,^{1,*} Ajay Kaladharan,^{1,†} and Yongcheng Wu^{2,‡}

¹*Department of Physics, Oklahoma State University, Stillwater, OK, 74078, USA*

²*Department of Physics and Institute of Theoretical Physics,
Nanjing Normal University, Nanjing, 210023, China*

Abstract

Supercooled first-order phase transition (FOPT) can lead to the formation of primordial black holes (PBHs). This scenario imposes stringent requirements on the profile of the effective potential. In this work, we use the singlet extended Standard Model (xSM) as a benchmark model to investigate this possibility at the electroweak scale. The PBHs formed during a supercooled FOPT have a narrow mass distribution around the mass of Earth. This distribution is closely tied to the temperature at which the PBHs form, corresponding to the FOPT at the electroweak scale. This scenario can be probed with microlensing experiments, space-based gravitational wave detectors, and collider experiments. Remarkably, the future space-based gravitational wave detector LISA will hold the potential to either confirm this PBH scenario in the xSM or completely rule it out for extremely small total dark matter fraction made of PBHs, down to $f_{\text{PBH}} > 10^{-300}$. Interestingly, our findings suggest that PBHs within the xSM framework may align with observations of the six ultrashort timescale events reported by the OGLE microlensing experiment.

*Electronic address: dorival@okstate.edu

†Electronic address: kaladharan.ajay@okstate.edu

‡Electronic address: ycwu@njnu.edu.cn

Contents

I. Introduction	3
II. The xSM model	5
III. Electroweak phase transition	6
IV. Primordial black holes from first-order phase transition	8
V. Results	13
A. PBH formation in the xSM and shape of the effective potential	13
B. Microlensing constraints	19
C. Gravitational wave experiments	21
D. Collider constraints	22
VI. Conclusion	24
Acknowledgments	25
A. Parametrization scan for xSM	26
B. Phenomenological constraints	27
C. Perturbative unitarity of the S-matrix	28
D. PBH calculation	30
E. Gravitational wave signatures	31
1. Sound waves	32
2. Bubble collisions	34
3. MHD turbulence	34
References	35

I. INTRODUCTION

Primordial black holes (PBHs) can be formed from the collapse of large density inhomogeneities in the early Universe [1–6]. Cosmological first-order phase transition may provide ideal conditions for PBH formation through the compression of large amount of energy into a small volume through bubble collisions [7–9], trapped particles [10–15], or delayed vacuum transition [16–28]. In this paper, we will focus on the latter scenario.

The probabilistic nature of bubble nucleation implies that there is the possibility that large regions may remain in the false vacuum state, where nucleation is delayed, and are surrounded by regions dominated by the true vacuum state. While the vacuum energy density remains almost constant, the radiation energy density decreases as the Universe expands. Therefore, the total energy density increases in the region where false vacuum decay is delayed relative to the background region. When the vacuum energy density inside those regions decays into other components, overdensity may reach a threshold, and the whole mass inside the region could gravitationally collapse into PBHs. In this scenario, PBHs can serve as both dark matter candidates and probe for models featuring first-order

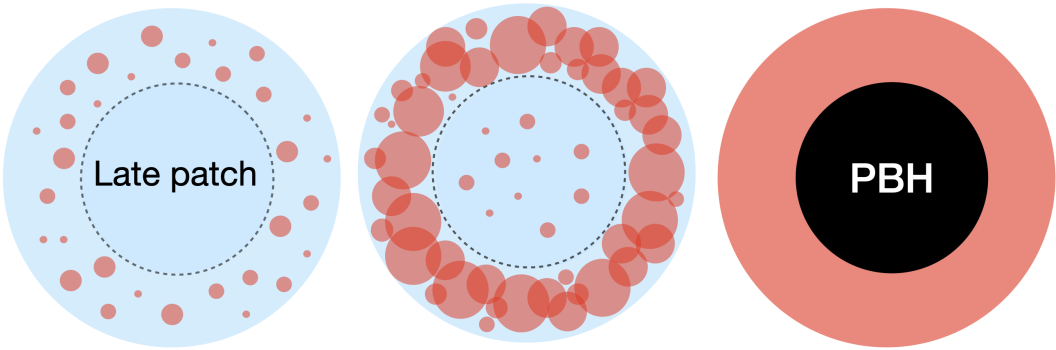


FIG. 1: PBH formation from collapse of delayed false vacuum patches. Left panel: Bubble nucleation, occurring randomly, may start later in certain causal patches compared to the surrounding regions. Central panel: In supercooled conditions, false vacuum regions in blue are vacuum-dominated, while true vacuum regions in red are energetically dominated by components that redshift akin to radiation. Thus, the background redshifts quickly, whereas the “late patch” maintains a nearly constant energy density. Right panel: As a result of the delayed nucleation of bubbles in the late patch, energy density within it surpasses that of the background region. When this overdensity crosses a critical threshold, it can collapse to form a PBH.

phase transitions, making it phenomenologically appealing, as we will illustrate in the present study. In Fig. 1, we summarize the process for PBH formation from collapse of delayed false vacuum patches.

In this work, we will demonstrate, for the first time, that this scenario of PBH formation can arise in the context of the relevant theoretical benchmark known as xSM. The xSM extends the Standard Model (SM) by introducing a new gauge singlet scalar. Our analysis reveals that this model can generate a wide range of dark matter fractions. Furthermore, the PBH mass spectrum in this model is highly constrained around 10^{-5} solar masses, reflecting a direct correlation with the temperature at which the PBHs form. Interestingly, the current OGLE experiment has detected six ultrashort timescale events that align with the characteristics expected of Earth-mass PBHs [29, 30]. Thus, PBH formation via a supercooled electroweak phase transition emerges as a potential explanation.

We will show that the PBH phenomenology will lead to novel and relevant constraints on this model from microlensing experiments, complementing constraints from collider experiments such as the High-Luminosity LHC (HL-LHC) [31–46], and future gravitational wave (GW) experiments such as the Laser Interferometer Space Antenna (LISA) [47]. Therefore, we will illustrate using the xSM, that models featuring a first-order electroweak phase transition can be comprehensively tested through a multipronged approach, including PBH phenomenology.

The remainder of the paper is organized as follows. We briefly introduce the xSM model in Sec. II. The electroweak phase transition in the xSM is discussed in Sec. III. Moving to Sec. IV, we analyze the mechanism of PBH formation during a delayed phase transition. The results in the xSM model will be presented in Sec. V. We start with a general discussion about the requirements of PBH formation to the structure of the Higgs potential. This is followed by the presentation of constraints from microlensing, gravitational waves, and collider experiments. We conclude in Sec. VI. Details about the parameter space scan, theoretical and experimental constraints to the xSM, PBH calculation, and the calculation of GW signal are provided in the Appendices.

II. THE XSM MODEL

In the xSM framework, the SM is extended by one real scalar field S , which is a singlet under the SM symmetry $SU(3)_C \otimes SU(2)_L \otimes U(1)_Y$ [31–34, 36, 37, 39, 40]. The general gauge-invariant scalar potential is given by

$$V(H, S) = -\mu^2 H^\dagger H + \lambda(H^\dagger H)^2 + \frac{a_1}{2} H^\dagger H S + \frac{a_2}{2} H^\dagger H S^2 + \frac{b_2}{2} S^2 + \frac{b_3}{3} S^3 + \frac{b_4}{4} S^4, \quad (1)$$

where H is the SM Higgs doublet, and all the model parameters in Eq. (1) are real. Expanding around the vacuum expectation values (VEVs), the Higgs doublet H and real scalar S can be written as

$$H = \begin{pmatrix} G^+ \\ \frac{v_{\text{EW}} + h + iG^0}{\sqrt{2}} \end{pmatrix}, \quad \text{and} \quad S = v_s + s, \quad (2)$$

where G^\pm and G^0 are the Goldstone fields, h and s are the Higgs and singlet scalars, $v_{\text{EW}} = 246 \text{ GeV}$, and v_s is the singlet VEV at zero-temperature. The minimization conditions around the electroweak (EW) vacuum at zero temperature allow parameters μ and b_2 in Eq. (1) to be expressed in terms of the VEVs and other parameters as

$$\mu^2 = \lambda v_{\text{EW}}^2 + \frac{1}{2} v_s (a_1 + a_2 v_s), \quad (3)$$

$$b_2 = -\frac{1}{4v_s} [v_{\text{EW}}^2 (a_1 + 2a_2 v_s) + 4v_s^2 (b_3 + b_4 v_s)]. \quad (4)$$

Using Eq. (4), the mass matrix for (h, s) can be written as

$$M_{h,s}^2 = \begin{pmatrix} 2\lambda v_{\text{EW}}^2 & \frac{1}{2} a_1 v_{\text{EW}} + a_2 v_{\text{EW}} v_s \\ \frac{1}{2} a_1 v_{\text{EW}} + a_2 v_{\text{EW}} v_s & v_s (b_3 + 2b_4 v_s) - \frac{v_{\text{EW}}^2}{4v_s} a_1 \end{pmatrix}. \quad (5)$$

The physical eigenstate (h_1, h_2) can be expressed in terms of gauge eigenstate (h, s) and mixing angle θ which diagonalizes the matrix in Eq. (5)¹

$$h_1 = c_\theta h + s_\theta s, \quad h_2 = -s_\theta h + c_\theta s, \quad (6)$$

where h_1 is identified as the 125 GeV SM Higgs boson while h_2 is a new scalar.

¹ Here $s_x \equiv \sin(x)$ and $c_x \equiv \cos(x)$.

The model parameters (λ, a_1, a_2) can be expressed in terms of physical parameters $(m_{h_1}, m_{h_2}, \theta)$ as

$$\lambda = \frac{m_{h_1}^2 c_\theta^2 + m_{h_2}^2 s_\theta^2}{2v_{\text{EW}}^2}, \quad (7)$$

$$a_1 = \frac{2v_s}{v_{\text{EW}}^2} [2v_s^2(2b_4 + \tilde{b}_3) - m_{h_1}^2 - m_{h_2}^2 + c_{2\theta}(m_{h_1}^2 - m_{h_2}^2)], \quad (8)$$

$$a_2 = \frac{-1}{2v_{\text{EW}}^2 v_s} \left[-2v_s(m_{h_1}^2 + m_{h_2}^2 - 4b_4 v_s^2) + (m_{h_1}^2 - m_{h_2}^2)(2c_{2\theta} v_s - v_{\text{EW}} s_{2\theta}) + 4\tilde{b}_3 v_s^3 \right], \quad (9)$$

where $\tilde{b}_3 \equiv b_3/v_s$. Therefore, the model can be fully specified using the following five free parameters:

$$v_s, \quad m_{h_2}, \quad \theta, \quad b_3, \quad b_4. \quad (10)$$

The details of the parametrization scan are provided in Appendix A.

By virtue of Eq. (6), the gauge and Yukawa couplings of h_1 and h_2 are scaled by a factor of c_θ and s_θ respectively with respect to the SM Higgs couplings

$$g_{h_1 XX} = c_\theta g_{h XX}^{\text{SM}}, \quad \text{and} \quad g_{h_2 XX} = -s_\theta g_{h XX}^{\text{SM}}, \quad (11)$$

where XX represents W^+W^- , ZZ , and $f\bar{f}$. The triple-Higgs coupling $\lambda_{111}h_1h_1h_1$ and the coupling between singlet and Higgs boson $\lambda_{211}h_2h_1h_1$ after electroweak symmetry breaking are given by [33]

$$\lambda_{111} = \frac{1}{2} \left[-s_\theta^3 \frac{b_3}{3} + s_\theta^2 \left(-\frac{v_{\text{EW}}}{v_s} c_\theta + \frac{1}{2} \frac{v_{\text{EW}}^2}{v_s^2} s_\theta \right) \frac{a_1}{2} + m_{h_1}^2 \left(\frac{s_\theta^3}{v_s} + \frac{c_\theta^3}{v_{\text{EW}}} \right) \right], \quad (12)$$

$$\begin{aligned} \lambda_{211} = & \frac{1}{4} [(a_1 + 2a_2 v_s) c_\theta^3 + 4v_{\text{EW}}(a_2 - 3\lambda) c_\theta^2 s_\theta \\ & - 2(a_1 + 2a_2 v_s - 2b_3 - 6b_4 v_s) c_\theta s_\theta^2 - 2a_2 v_{\text{EW}} s_\theta^3]. \end{aligned} \quad (13)$$

Theoretical and experimental constraints for the xSM model used in this analysis are detailed in Appendix B.

III. ELECTROWEAK PHASE TRANSITION

The dynamics of electroweak symmetry breaking in the early Universe is governed by the effective potential. In the xSM, the barrier is generated primarily by tree-level cubic terms [43, 48]. As tree-level terms drive the electroweak phase transition (EWPT), it is possible to perform a gauge invariant high-temperature expansion equivalent to considering

only the thermal mass corrections [49–56]. The gauge invariant effective potential is given by

$$V_{\text{eff}}(h, s, T) = \frac{1}{2}[-\mu^2 + \Pi_h T^2]h^2 + \frac{1}{2}[b_2 + \Pi_s T^2]s^2 + \frac{\lambda}{4}h^4 + \frac{a_1}{4}h^2s + \frac{a_2}{4}h^2s^2 + \frac{b_3}{3}s^3 + \frac{b_4}{4}s^4, \quad (14)$$

where $\Pi_h T^2$ and $\Pi_s T^2$ are the thermal masses of the fields, with coefficients given by

$$\Pi_h = \left(\frac{2m_W^2 + m_Z^2 + m_t^2}{4v_{\text{EW}}^2} + \frac{\lambda}{2} + \frac{a_2}{24} \right), \quad (15)$$

$$\Pi_s = \left(\frac{a_2}{6} + \frac{b_4}{4} \right), \quad (16)$$

where m_W , m_Z , and m_t are the masses of W -boson, Z -boson and top quark, respectively. The xSM model exhibits both one-step and two-step phase transitions. In this study, we examine the potential PBH formation for both of these cases.

In the SM, electroweak symmetry breaking occurs via a smooth crossover transition [57]. However, the introduction of new physics could convert it to a first-order phase transition. In this scenario, the phase transition proceeds through thermal tunneling from false to true vacua. This process leads to the emergence and expansion of bubbles of the broken phase within the surrounding region of the symmetric phase, effectively converting the false vacuum into true vacuum. The tunneling probability is provided by [58, 59]

$$\Gamma(T) \approx T^4 \left(\frac{S_3}{2\pi T} \right)^{3/2} e^{-\frac{S_3}{T}}, \quad (17)$$

where S_3 denotes the three-dimensional Euclidean action corresponding to the formation of the critical bubble

$$S_3 = 4\pi \int_0^\infty dr r^2 \left[\frac{1}{2} \left(\frac{d\phi(r)}{dr} \right)^2 + V(\phi, T) \right]. \quad (18)$$

Here, the critical bubble profile ϕ is obtained by solving the following differential equation

$$\frac{d^2\phi}{dr^2} + \frac{2}{r} \frac{d\phi}{dr} = \frac{dV(\phi, T)}{d\phi}, \quad \text{with} \quad \lim_{r \rightarrow \infty} \phi(r) = 0 \quad \text{and} \quad \lim_{r \rightarrow 0} \frac{d\phi(r)}{dr} = 0. \quad (19)$$

We employ the publicly available code `CosmoTransitions` [60] to solve the differential equation Eq. (19) and subsequently evaluate the Euclidean action S_3 . The first-order phase transition is considered nearly complete around the nucleation temperature T_n , at which one bubble nucleates per unit horizon volume [61]

$$\int_{T_n}^\infty \frac{dT}{T} \frac{\Gamma(T)}{H(T)^4} = 1. \quad (20)$$

Strong first-order phase transition can generate stochastic gravitational wave signals. These GW signals emerge from three sources: vacuum bubble collision, fluid motion in the plasma resembling sound waves, and turbulent motion within the plasma. In this work, we are interested in the parameter space that leads to PBH formation, coinciding with a supercooling phase transition. In this scenario, it is more robust to consider the percolation temperature T_p , when 29% of space is covered by true vacuum bubbles, as the transition temperature for evaluating the gravitational signal [62–65].

One important parameter which influences the GW signal is α , which denotes the ratio of vacuum energy density Λ_{vac} released as latent heat during phase transition to the radiation energy density ρ_{rad} .² The vacuum energy density, radiation energy density, and α are given by

$$\Lambda_{\text{vac}} = \Delta \left(-V_{\text{eff}} + T \frac{\partial V_{\text{eff}}}{\partial T} \right), \quad \rho_{\text{rad}} = \frac{\pi^2}{30} g_{\star} T^4, \quad \text{and} \quad \alpha = \left. \frac{\Lambda_{\text{vac}}}{\rho_{\text{rad}}} \right|_{T=T_p}, \quad (21)$$

where $g_{\star} = 106.75$ denotes the number of relativistic degrees of freedom in the plasma and Δ denotes the difference between the true and false vacua. The calculation details for the GW energy density $\Omega_{\text{GW}} h^2$ are provided in Appendix E.

IV. PRIMORDIAL BLACK HOLES FROM FIRST-ORDER PHASE TRANSITION

PBHs can be formed from the collapse of large density inhomogeneities in the early Universe [1–4]. In this study, we focus on PBH formation due to a delayed vacuum transition [16–28]. The probabilistic nature of bubble nucleation implies that some large regions may remain longer in a false vacuum state, surrounded by areas that have transitioned to the true vacuum state. While the vacuum energy density remains approximately constant, the radiation energy density decreases as $a(t)^{-4}$ when the Universe expands. Hence, the total energy density in regions with delayed vacuum decay increases compared to surrounding regions where the decay occurs earlier. The resulting overdensity can reach a critical

² For a more comprehensive analysis, the parameter β , commonly employed in modelling GW signals in the literature, is replaced by length scale $R_{\star} = (8\pi)^{\frac{1}{3}} \frac{v_w}{\beta}$, which represents the mean separation of bubbles. The details of the evaluation of R_{\star} are provided in Appendix E.

threshold, causing the entire mass of the region to gravitationally collapse into PBHs, as illustrated in Fig. 1.

In general, the expected volume of true vacuum bubbles per comoving volume is given by [66]

$$I(t) = \frac{4\pi}{3} \int_{t_0}^t dt' \Gamma(t') a^3(t') r^3(t, t'), \quad (22)$$

where t_0 is the time when the first bubble is nucleated, and $r(t, t') \equiv v_w \int_{t'}^t a(t)^{-1} dt$ is the comoving radius of a bubble nucleated at time t' and observed at t . We assume the velocity of the bubble wall close to the speed of light $v_w \approx 1$.³ $I(t)$ overestimates the fraction of true vacuum bubbles, as it double counts the overlap region and also includes fictitious nucleation in the true vacuum [66, 69]. The probability that a given point in the comoving volume remains in the false vacuum is given by [17, 66, 70]

$$F(t) = \begin{cases} 1, & \text{if } t < t_0, \\ e^{-I(t)}, & \text{if } t \geq t_0, \end{cases} \quad (23)$$

where the exponential compensates the double counting mentioned above. Before the nucleation of the first bubble at t_0 , the entire space is covered by a false vacuum; therefore, $F(t) = 1$ for $t < t_0$ and $F(t)$ decreases as the true vacuum bubble nucleates and expands. With this probability, the percolation time t_p (and equivalently the corresponding percolation temperature T_p) is defined as the point when the false vacuum fraction drops below the threshold $F(t_p) \simeq 0.71$.

The evolution of the Hubble scale factor is determined by the Friedmann equation [71]

$$H^2 = \left(\frac{1}{a} \frac{da}{dt} \right)^2 = \frac{1}{3M_{\text{Pl}}^2} (\rho_V + \rho_r + \rho_w), \quad (24)$$

where ρ_V , ρ_r , and ρ_w are the energy densities for the false vacuum, background radiation, and bubble wall, respectively, and $M_{\text{Pl}} = 2.435 \times 10^{18}$ GeV [70]. The vacuum energy density ρ_V is given by

$$\rho_V = F(t) \Lambda_{\text{vac}}(t), \quad (25)$$

where Λ_{vac} is the energy density difference between false and true vacuum at time t , as defined in Eq. (21). Given that the bubble wall velocity is assumed to be close to the speed of light,

³ The Chapman-Jouguet velocity [67, 68] in Eq. (E14) sets the lower limit for the bubble wall velocity. For $\alpha = 1$ (10), the Chapman-Jouguet velocity is 0.934 (0.991). In our investigation, we are more interested in the $\alpha \gg 1$ regime, where the Chapman-Jouguet velocity approaches unity.

the bubble wall can be effectively treated as radiation [22]. Therefore, the total radiation energy density is the sum of the background radiation and the bubble wall contributions

$$\rho_R = \rho_r + \rho_w, \quad (26)$$

and the evolution of radiation energy density is described by

$$\frac{d\rho_R}{dt} + 4H\rho_R = -\frac{d\rho_V}{dt}. \quad (27)$$

In particular, Eq. (27) shows that as $F(t)$ decreases from 1 to 0, the vacuum energy is converted to radiation.

We consider a region where nucleation of the first bubble is delayed to time t_i , referred to as *late patch*. The average spatial fraction of the false vacuum in this region is obtained from Eq. (22) and Eq. (23) with the delayed nucleation time

$$F_{\text{in}}(t) = \begin{cases} 1, & t < t_i \\ \exp \left[-\frac{4\pi}{3} \int_{t_i}^t dt' \Gamma(t') a_{\text{in}}^3(t') \left(\int_{t'}^t \frac{d\tilde{t}}{a_{\text{in}}(\tilde{t})} \right)^3 \right], & t \geq t_i \end{cases} \quad (28)$$

where a_{in} is the scale factor of the *late patch*. Similarly, the fraction of false vacuum for the background region F_{out} can be evaluated with the nucleation time $t_0 = t_c$. Due to the delayed nucleation of bubbles in the late patch, the energy density in the *late patch* is higher than in the background region. This energy contrast can be quantified as [17, 20]

$$\delta = \frac{\rho^{\text{in}} - \rho^{\text{out}}}{\rho^{\text{out}}}. \quad (29)$$

If the energy contrast exceeds the critical threshold, $\delta_c = 0.45$ [72, 73], the *late patch* gravitationally collapses into PBH. For a given t_i , we find the t_{PBH} time at which δ reaches the threshold value $\delta_c = 0.45$ and PBH is formed.

The probability of the *late patch* remaining in the false vacuum until t_i is given by [17, 20, 23]

$$P(t_i) = \exp \left[- \int_{t_c}^{t_i} dt' \Gamma(t') a_{\text{in}}(t')^3 V_{\text{coll}} \right], \quad (30)$$

where the volume factor V_{coll} is defined by [20]

$$V_{\text{coll}} = \frac{4\pi}{3} \left[\frac{1}{a_{\text{in}}(t_{\text{PBH}}) H_{\text{in}}(t_{\text{PBH}})} + \int_{t'}^{t_{\text{PBH}}} \frac{d\tilde{t}}{a_{\text{out}}(\tilde{t})} \right]^3. \quad (31)$$

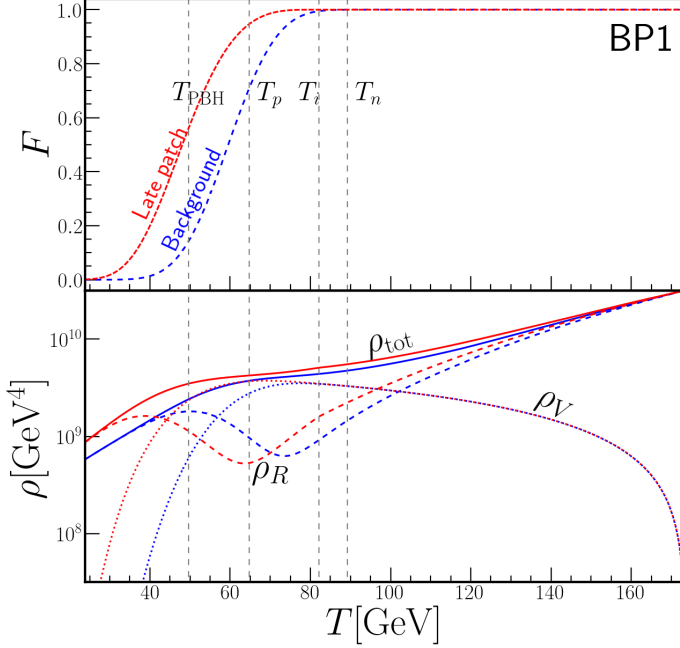


FIG. 2: In the top panel, we present the fraction of false vacuum inside and outside the late Hubble volume as a function of temperature for BP1, as defined in Tab. I. In the bottom panel, we show the evolution of energy density with temperature for both the background region and the late patch. In this panel, the dashed lines represent the radiation component, while the dotted lines indicate the vacuum energy density component.

The second term in Eq. (31) represents the radius of the bubble nucleated at t' by the time t_{PBH} . Including this term in Eq. (31) ensures that no large bubble nucleated in the surrounding background patch enters the *late patch* before its collapse at t_{PBH} [22].

The mass of PBH can be roughly approximated as the Hubble horizon mass at the temperature when the PBHs are produced [17–19, 74]

$$M_{\text{PBH}} \approx \frac{4\pi}{3} H_{\text{in}}^{-3}(t_{\text{PBH}}) \rho_c = 4\pi M_{\text{Pl}}^2 H_{\text{in}}^{-1}(T_{\text{PBH}}), \quad (32)$$

where ρ_c is the critical density. If we regard PBH as a component of dark matter (DM) [75], the fraction of the PBH from the first-order phase transition in dark matter density is given by [18, 19]

$$f_{\text{PBH}} \equiv \frac{\rho_{\text{PBH}}}{\rho_{\text{DM}}} = \left(\frac{H(t_{\text{PBH}})}{H(t_0)} \right)^2 \left(\frac{a(t_{\text{PBH}})}{a(t_0)} \right)^3 P(t_i) \frac{1}{\Omega_{\text{DM}}}, \quad (33)$$

where t_0 is the present time. For the electroweak phase transition f_{PBH} can be approximated

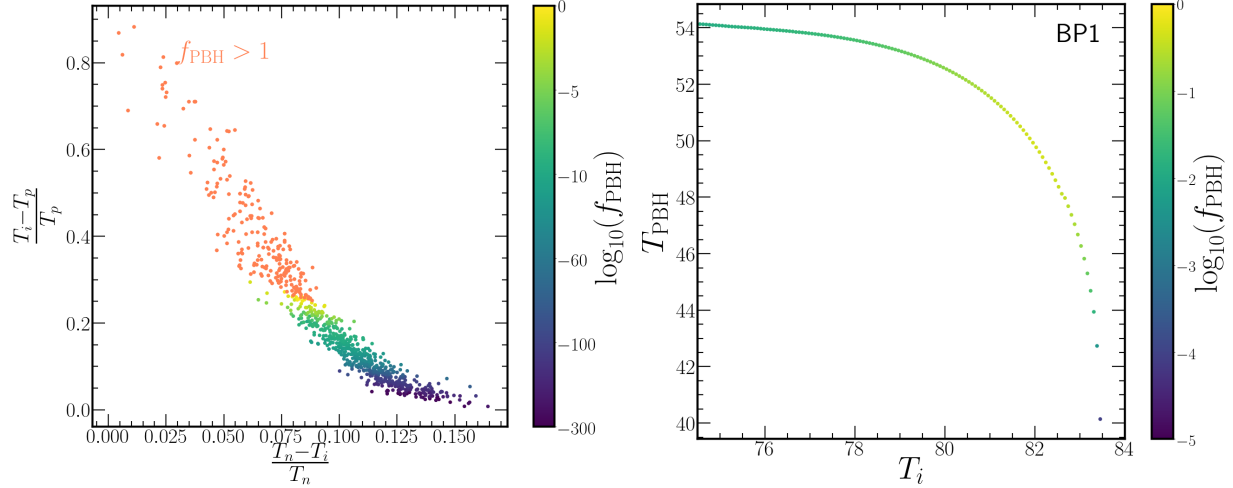


FIG. 3: In the left panel, we show $(T_n - T_i)/T_n$ versus $(T_i - T_p)/T_p$ color-coded with f_{PBH} . The points overproducing PBH, $f_{\text{PBH}} > 1$, are shown in orange. The values of T_i are obtained maximizing $P(T_i)$ thereby f_{PBH} . As T_i approaches T_p , the value of f_{PBH} exponentially decreases. Conversely, when T_i approaches T_n , PBHs are overproduced, $f_{\text{PBH}} > 1$. In the right panel, we present T_i and the corresponding T_{PBH} color-coded with f_{PBH} for BP1. As T_i increases, f_{PBH} reaches a maximum value and then decreases.

as

$$f_{\text{PBH}}^{\text{EW}} \sim 1.52 \times 10^{11} \left(\frac{0.245}{\Omega_{\text{DM}}} \right) \left(\frac{T_{\text{PBH}}}{100 \text{ GeV}} \right) P(T_i), \quad (34)$$

where $\Omega_{\text{DM}} = 0.245$ is the present dark matter density normalized by total energy density.^{4,5}

In Fig. 2, we illustrate the phenomenology described above using the xSM benchmark point 1 (BP1) listed in Tab. I. The top panel compares the evolution of the false fraction vacuum with temperature in the *background region* F_{out} , where nucleation begins at T_n , to the evolution in the *late patch* F_{in} , where it is delayed to T_i . The bottom panel depicts

⁴ PBHs with masses below $10^{-19} M_{\odot}$ are expected to have evaporated by the present time due to Hawking radiation [76]. However, PBHs formed during the electroweak transition typically have masses around $10^{-6} M_{\odot}$. Estimates suggest that the impact of Hawking radiation on the mass of these PBHs is negligible. As a result, the overall mass of PBHs, and consequently their contribution to the dark matter density, remains largely unaffected.

⁵ PBHs can accrete primordial gas in the early Universe, converting a fraction of this mass into radiation. This additional energy injection into the plasma can affect its thermal and ionization histories, leading to changes in the cosmic microwave background (CMB) frequency spectrum [77]. These effects are subleading for PBHs formed during EWPT as considered in the present study, which typically have masses around $10^{-6} M_{\odot}$, being relevant for PBHs with masses $\gtrsim 10^2 M_{\odot}$ [78].

the evolution of the energy density for both the background and late patch regions. Both the background and late patch vacuum energies are converted into radiation, however, the background transitions earlier making it to redshift quickly, whereas the late patch retains vacuum-dominated regions for a longer duration. This behavior results in an increase in δ as the vacuum decays in the late patch, ultimately reaching the PBH formation threshold at $\delta_c = 0.45$, which defines T_{PBH} .

For the numerical analysis, we determine T_i by identifying the temperature that maximizes the PBH abundance f_{PBH} Eq. (33), scanning over the range $T_p < T_i < T_n$ [23]. The left panel of Fig. 3 justifies this scanning procedure. For $T_i < T_p$, the value of f_{PBH} will be extremely small, $f_{\text{PBH}} \ll 10^{-300}$, and for $T_i > T_n$, the parameter points would be non-physical due to overproduction of PBH, $f_{\text{PBH}} > 1$. In the right panel of Fig. 3, we illustrate this behavior for BP1 by presenting T_i and corresponding value of T_{PBH} , color-coded with f_{PBH} . The value of f_{PBH} increases with T_i , and it reaches a threshold around 82.10 GeV. After this point, f_{PBH} drops due to a substantial decrease in T_{PBH} . Additional details on the PBH calculation, initial conditions for the evolution of energy densities, and translation into temperature coordinates are provided in Appendix D.

V. RESULTS

The xSM model displays both single and multiple-step phase transitions. In this study, we comprehensively examine all possible phase transition patterns, with a focus on transitions resulting in PBH formation. In our parameter space analysis, we observe that 78.9% of the parameter space points show PBH formation with a single-step phase transition.⁶ This phase transition pattern is illustrated by the benchmark points BP1-BP3 in Tab. I. The remaining 21.1% points enjoy a two-step phase transition. BP4 in Tab. I is one such benchmark illustrating this scenario.

A. PBH formation in the xSM and shape of the effective potential

In this section, we examine the profile required in the effective potential of the xSM model that triggers the formation of PBHs. In Fig. 4, we show $(T_n - T_p)/T_n$, which quantifies the

⁶ See Appendix A for more details on the parameter space scan.

	BP1	BP2	BP3	BP4	BP5
v_s [GeV]	429.490	503.45	641.44	1045.66	480.429
m_{h_2} [GeV]	742.534	817.06	835.065	1144.538	945.846
θ	-0.1597	-0.015458	-0.15763	-0.00208	-0.1548
b_3 [GeV]	-2509.635	-2348.49	-1990.700	-2130.053	-2272.226
b_4	4.149478	3.474019	2.28183	1.5696	3.4788
T_n [GeV]	89.20	101.82	125.91	190.61	117.98
T_P [GeV]	64.78	75.71	92.41	142.46	114.09
T_i [GeV]	82.10	92.58	116.66	177.45	NA
T_{PBH} [GeV]	59.53	30.65	71.30	109.167	NA
$f_{\text{PBH}}^{\text{EW}}$	0.457	1.544×10^{-5}	0.02263	4.368×10^{-5}	NA
α	6.31	4.525	4.423	3.65	0.645
R_\star [GeV $^{-1}$]	4.52×10^{13}	2.99×10^{13}	2.95×10^{13}	1.21×10^{13}	2.76×10^{12}

TABLE I: Benchmark points for the singlet scalar model. BP1, BP2, and BP3 exemplify a single-step phase transition. BP4 is an example of two-step phase transition. BP5 does not lead to PBH formation, and is defined to highlight the importance of the U-shape profile presented in Fig. 5.

extent of supercooling versus α evaluated at T_p for the parameter points that show PBH formation. It is clear that PBH forms only if we have sufficient supercooling $(T_n - T_p)/T_n \gtrsim 0.12$. However, if the supercooling is too large $(T_n - T_p)/T_n \gtrsim 0.3$, the PBH is overproduced and can overclose the Universe. Within the viable range, the amount of PBH formed is highly sensitive to the extent of supercooling with only a minor dependence on α , as supercooling exponentially affects the probability of PBH formation.

To investigate the primary factors that trigger supercooling, we analyze the evolution of S_3/T as a function of temperature for two benchmark points: BP2 and BP5. Details regarding these BPs are provided in Tab. I. The left panel of Fig. 5 illustrates the evolution of S_3/T with temperature for BP2, which exhibits PBH formation. Notably, S_3/T displays a U-shaped behavior with temperature, leading to an exponential suppression of the tunneling rate at both high and low temperatures [39]. This suppression enables significant bubble formation only within a specific intermediate temperature range. In this scenario,

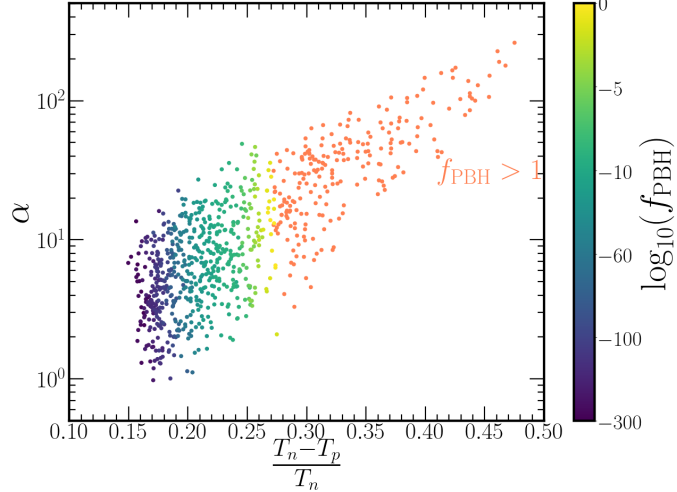


FIG. 4: We present the supercooling parameter $(T_n - T_p)/T_n$ plotted against α evaluated at T_p , with color coding indicating the value of f_{PBH} . Parameter points exhibiting PBH overproduction with $f_{\text{PBH}} > 1$ are represented in orange.

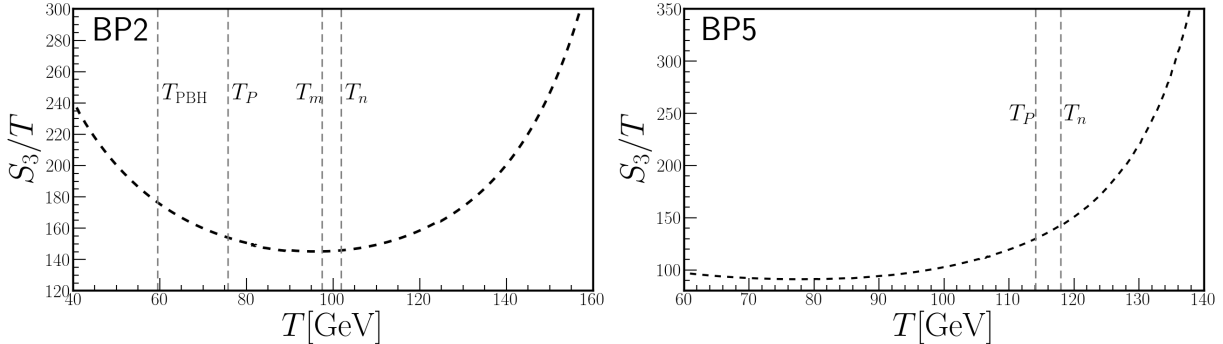


FIG. 5: The evolution of S_3/T with temperature for the BP2 (left panel) and BP5 (right panel), as defined in Tab. I. BP2 exhibits a U-shaped behavior of S_3/T near the nucleation temperature, whereas BP5 does not show this profile. BP1 undergoes significant supercooling, resulting in PBH formation. In contrast, BP5 experiences minimal supercooling and does not lead to PBH formation. The nucleation temperature T_n and percolation temperature T_p are depicted with dotted lines. Furthermore, for BP2, we have indicated the PBH formation temperature T_{PBH} and the temperature where the tunneling rate is maximum T_m .

the tunneling rate can be approximated by [28, 62, 65]

$$\Gamma = \Gamma_0 e^{-\frac{1}{2}\beta V(T-T_m)^2}, \quad (35)$$

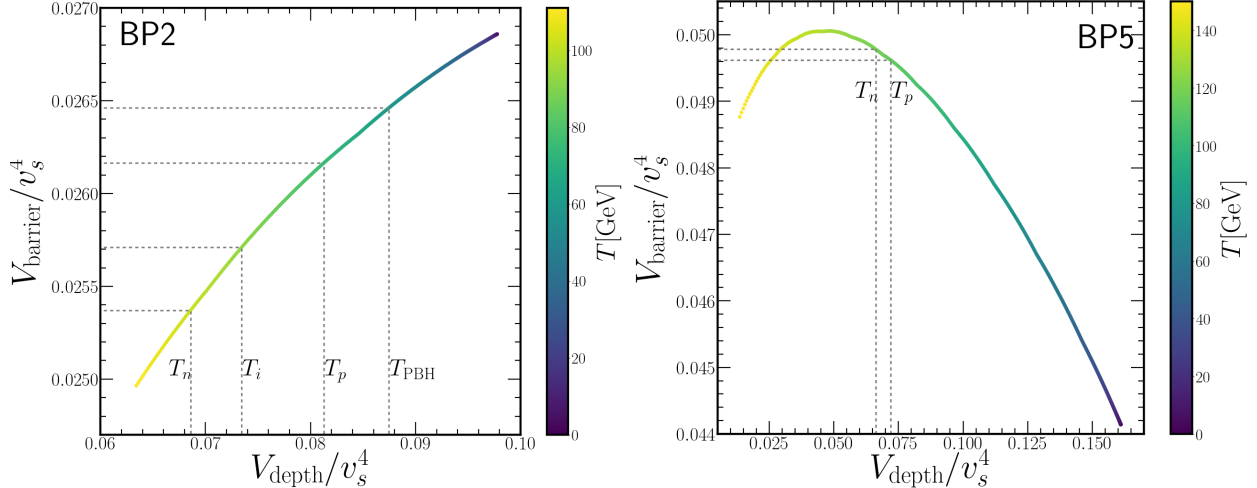


FIG. 6: We show the thermal evolution of the shape of the potential by plotting V_{barrier} versus V_{depth} color-coded with temperature for the BP2 (left panel) and BP5 (right panel) provided in Tab. I. The benchmark point BP2 show U-shaped behavior for S_3/T near nucleation temperature, while BP5 does not show such behavior. For BP1, the height of the barrier increases with temperature, while for BP5, the height decreases with temperature, exhibiting a distinctive behavior.

where T_m is the temperature at which tunneling rate is maximum and $\beta_V \equiv \frac{d^2(S_3/T)}{dT^2} \Big|_{T=T_m}$. This characteristic behavior of S_3/T and subsequently of the tunneling rate leads to a supercooling phase transition, which helps the production of PBHs. In contrast, the right panel of Fig. 5 shows the temperature evolution of S_3/T for BP5, which does not present significant supercooling and does not result in PBH formation. BP5 lacks the U-shaped behavior of S_3/T near the nucleation temperature. Hence, the tunneling rate increases steadily between the temperatures T_n and T_p , leading to bubble percolation shortly after the nucleation of the first bubble.

In some model-agnostic studies of PBH formation from first-order phase transition [17, 20], the tunneling rate, given by Eq. (17), is often approximated by $\Gamma(t) \approx \Gamma_0 e^{\beta(t-t_n)}$, where Γ_0 is the value of tunneling rate at the nucleation time t_n and $\beta \equiv -dS_3(t)/dt|_{t=t_n}$. However, it is evident from the Fig. 5 that such an approximation may not consistently hold for the xSM model and other models which have a significant zero-temperature barrier. This is because the U-shaped behavior of S_3/T near T_n is not captured by this simple exponential approximation. Thus, it is more appropriate to use the tunneling rate in Eq. (35), when S_3/T exhibits this U-shaped behavior around T_n .

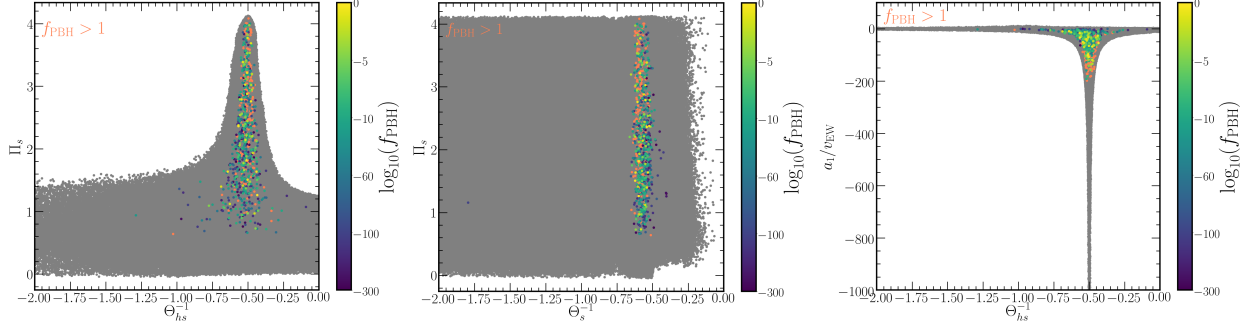


FIG. 7: We show the inverse of ratios Θ_{hs} and Θ_s versus thermal mass Π_s color coded by $\log_{10}(f_{\text{PBH}})$ for the center and right panel respectively. In the right panel we show the inverse of Θ_{hs} versus a_1 normalized by v_{EW} . Parameter points satisfying theoretical and experimental constraints are denoted in gray, whereas those exhibiting PBH formation with $T_i > T_p$ are highlighted in black and orange color denotes the parameter excluded due to overproduction of DM $f_{\text{PBH}} > 1$. Parameter points that lead to PBH formation have thermal mass $\Pi_s \gtrsim 0.8$, negative cubic couplings, and the values for Θ_{hs}^{-1} and Θ_s^{-1} are roughly in the vicinity of -0.5 and -0.57 .

To gain further insight into the scenarios that could result in the U-shaped behavior of S_3/T with temperature, we scrutinize the shape of the potential at finite temperature, focusing on barrier formation and vacuum upliftment [43, 44, 46]. In Fig. 6, we illustrate the thermal evolution of the barrier and the depth of the true vacuum for the BP2. For simplicity, the barrier is calculated along the line that directly connects the false and true vacuum. As the temperature cools down, both depth and barrier increase. The increase in barrier height makes tunneling from the false to true vacuum more challenging; as a consequence, we observe the U-shaped behavior for S_3/T behavior for BP2, as indicated in Fig. 5. The 83.2% of the parameter points that lead to PBH have this behavior where the barrier height increases between T_n and T_p , which serves as a sufficient condition for the U-shaped behavior of S_3/T with temperature.

From the observations in Fig. 6, it becomes apparent that the tree-level barrier plays a crucial role in the formation of PBHs in the xSM. The cubic terms in the Eq. (1) provide the dominant contribution to the barrier at zero temperature. We define the cubic terms normalized by the quartic terms as

$$\Theta_{hs} \equiv \frac{a_1}{a_2 v_s}, \quad \Theta_s \equiv \frac{4b_3}{3b_4 v_s}. \quad (36)$$

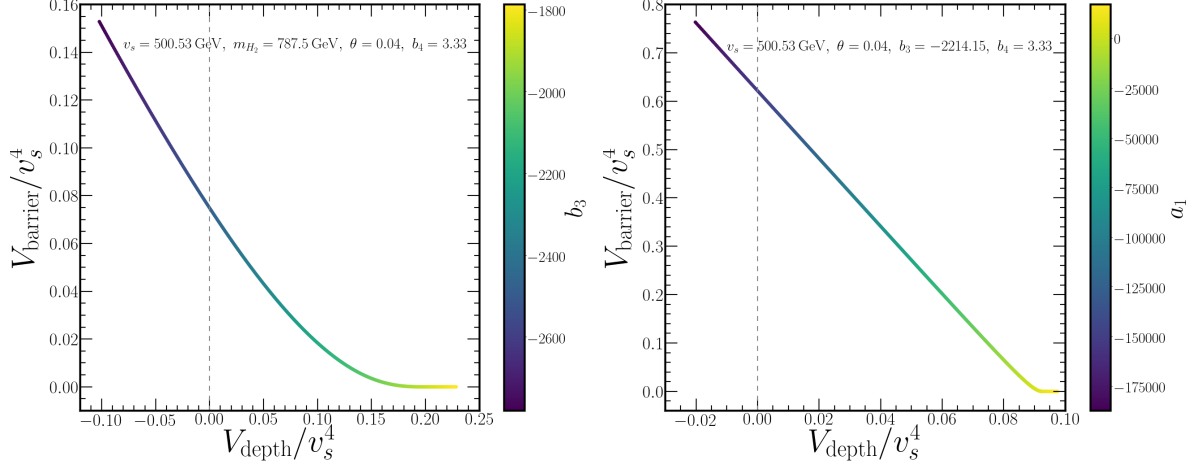


FIG. 8: We show the dependence of cubic terms b_3 (left panel) and a_1 (right panel) on the shape of potential at zero temperature by plotting V_{barrier} versus V_{depth} for different values of b_3 and a_1 . For the left panel, we fixed $v_s = 500.53 \text{ GeV}$, $m_{h_2} = 787.5 \text{ GeV}$, $\theta = 0.04$, and $b_4 = 3.33$. As the values of b_3 increase, the height of the barrier decreases, and eventually, the barrier disappears. For the large negative value of b_3 , the EW vacuum stability can be violated, as the depth reaches negative values. For the right panel we fixed $v_s = 500.53 \text{ GeV}$, $\theta = 0.04$, $b_3 = -2214.15$ and $b_4 = 3.33$. A similar trend emerges for a_1 : as cubic terms grow more negative, the barrier height increases while the depth decreases.

In the left (center) panel of the Fig. 7, we show Θ_{hs}^{-1} (Θ_s^{-1}) versus thermal mass Π_s color-coded by the $\log_{10}(f_{\text{PBH}})$. In the right panel, we show the cubic term a_1 normalized by the v_{EW} versus Θ_{hs}^{-1} color coded by the $\log_{10}(f_{\text{PBH}})$. The gray color denotes the parameter points that satisfy theoretical and experimental constraints, while those displaying PBH formation follow the color code associated with $\log_{10}(f_{\text{PBH}})$. The PBHs favor the parameter region with thermal mass $\Pi_s \gtrsim 0.8$, while the normalized cubic terms have relatively narrow allowed ranges: $\Theta_{hs}^{-1} \simeq -0.5$ and $\Theta_s^{-1} \simeq -0.57$. The PBH formation requires the cubic term to be negative and the corresponding quartic term to be positive.

This sensitive dependence of the PBH formation on Θ_{hs} and Θ_s can also be related to the influence of the cubic terms on the barrier and depth of the effective potential. To illustrate it, in the left panel of Fig. 8, we examine the shape of the potential at zero temperature by fixing $v_s = 500.53 \text{ GeV}$, $m_{h_2} = 787.5 \text{ GeV}$, $\theta = 0.04$, and $b_4 = 3.33$, while varying b_3 , which is equivalent to varying Θ_s . The height of the barrier and depth of the EW broken vacuum

are inversely correlated. As b_3 becomes increasingly negative, the cubic term dominates over the quartic term, the EW broken vacuum is uplifted compared to the EW symmetric vacuum and thereby, its depth decreases. On the other hand, the domination of the cubic term leads to the increase in the barrier height. As the value of b_3 becomes more negative, the depth decreases, and the height of the barrier increases. Around $b_3 \approx -2474$ ($\Theta_s^{-1} \approx -0.506$), depth becomes negative and the stability of the EW vacuum is violated. Hence, in view of the values of Θ_s^{-1} leading to PBH formation shown in Fig. 7, PBH generation favors parameter space where the potential has a shallow EW vacuum and sufficiently high barrier. A similar pattern can also be found for a_1 in the right panel of Fig. 8; as cubic terms become more negative, the barrier increases, and depth decreases. In the majority of the parameter space conducive to PBH formation, it is observed that both cubic couplings, b_3 and a_1 , collectively contribute to the generation of the barrier.

B. Microlensing constraints

The gravitational effects of the PBHs can be observed through its microlensing effects. In Fig. 9, we present the fraction of the contribution of PBHs to dark matter density today, f_{PBH} , as a function of the PBH mass derived from the xSM framework together with microlensing constraints from several experiments.⁷ In Fig. 9, the current microlensing constraints from Kepler [79], MACHO [80], EROS [81], SUBARU-HSC [82, 82, 83], and OGLE [29, 84, 85] are depicted with solid lines. Some comments are in order. First, the mass distribution of PBHs is remarkably narrow, approximately 10^{-5} solar masses. This narrow distribution is closely related to the temperature at which these PBHs form, as evidenced by Eq. (32), which aligns with the formation of PBH from first-order phase transition at the electroweak scale. Second, while the model in principle allows for the generation of significant dark matter fractions from PBHs, potentially reaching nearly 100% of the dark matter density, the large f_{PBH} regions are constrained by microlensing experiments. This implies that the contribution of PBHs to the dark matter density in this model can be as high as $f_{\text{PBH}} \approx 10^{-1}$, with OGLE, Subaru-HSC, and Eros experiments placing the most stringent limits [29, 81, 83, 87].

⁷ The microlensing constraints for the PBH are obtained from `PBHbounds` at <https://github.com/bradkav/PBHbounds>.

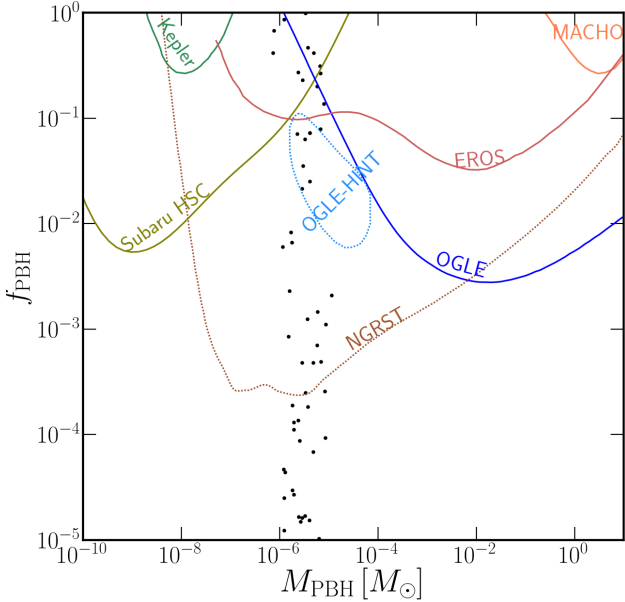


FIG. 9: Fraction of PBH contribution to dark matter density today $f_{\text{PBH}} \equiv \rho_{\text{PBH}}/\rho_{\text{DM}}$ as a function of the PBH mass $M_{\text{PBH}}[M_{\odot}]$ in the xSM model, where M_{\odot} is the solar mass. In addition, we present the microlensing constraints from Kepler [79], MACHO [80], EROS [81], SUBARU-HSC [82, 82, 83], and OGLE [29, 84, 85]. We also include the projected sensitivity of NGRST [86] and early hints of observation of Earth-sized PBHs by OGLE [29], indicated by dotted lines.

The OGLE experiment, through its 5-year observations of stars in the Galactic bulge, detected six ultrashort timescale events, hinting at the possible presence of Earth-sized PBH in the outer solar system [29, 30]. Alternatively, these events could also be linked to the new population of free-floating planets, one of which may have been captured by the solar system. Within the parameter space of the extended xSM, PBH formation is feasible, aligning well with the OGLE observations; for instance, benchmark point BP3 in Tab. I exemplifies this correspondence. This PBH parameter space could be explained using PBH produced from inflation [88–93], the collapse of domain wall [94] and axion star [95], but this is the first time, as per our knowledge, the OGLE-hint can be attributed to electroweak phase transition in a realistic BSM model that generates PBHs from delayed vacuum transition.

The forthcoming Nancy Grace Roman Space Telescope (NGRST), scheduled for launch in 2027, offers promising prospects for further investigating the PBH hypothesis concerning the six ultrashort timescale events detected by OGLE [86]. In Fig. 9, we present the sensitivity of NGRST and OGLE-hint with dotted lines. The NGRST has the sensitivity to probe

PBH with a dark matter fraction as low as 10^{-4} . Confirmation of the PBH explanation for ultrashort timescale events by these experiments could lead us to the favored parameter space in BSM theories that undergo EWPT with significant supercooling. Alternatively, if this scenario is ruled out, the high sensitivity of NGRST and other microlensing experiments will impose stringent constraints not only on the parameter space of the xSM model but also on similar models that induce PBH formation through delayed EW phase transitions.

C. Gravitational wave experiments

In the region favoring PBH formation, the large energy release during the phase transition results in detectable gravitational wave signals. For more details on the GW calculation, see the end of Sec. III and Appendix E. In Fig. 10, we show the maximum amplitude of gravitational waves produced during first-order phase transition as a function of its peak frequency, color coded by the PBH fraction f_{PBH} . Additionally, we provide the projected sensitivity curves for LISA [96], BBO [97] and three stages of DECIGO [98] GW experiments. PBH formation from first-order phase transition requires supercooling and a large value of

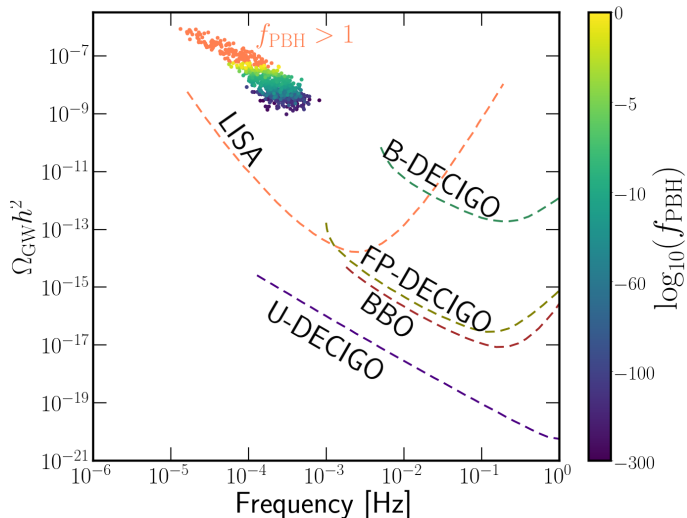


FIG. 10: The maximum amplitude of the gravitational wave spectrum as a function of peak frequency color coded by f_{PBH} and the orange color denotes the parameter excluded due to overproduction of DM $f_{\text{PBH}} > 1$. We also present the experimental sensitivities for LISA [96], BBO [97], and three stages of DECIGO [98]. The sensitivity from LISA was evaluated considering the duration of the mission of 5 years [96].

α , which coincides with promising gravitational wave signatures. Since the phase transition occurs at the electroweak scale, it naturally falls within the frequency range detectable by LISA. We find that all parameter points demonstrating PBH formation with $f_{\text{PBH}} > 10^{-300}$ in the xSM model can be probed by LISA. Consequently, LISA will have the potential to either confirm this PBH scenario or completely rule it out, down to these infinitesimally small values of f_{PBH} .

D. Collider constraints

PBH formation is favored in regions of parameter space leading to a large barrier at zero temperature, requiring specific cubic couplings, as discussed in Sec. V A. This results in distinct triple Higgs couplings λ_{111} , which can provide relevant LHC phenomenology, as we will demonstrate. In the left panel of Fig. 11, we show triple Higgs coupling modifier, $\kappa_\lambda = \lambda_{111}/\lambda_{111}^{\text{SM}}$, as a function of the heavy Higgs mass m_{h_2} . The projected sensitivity at the HL-LHC, with 3 ab^{-1} integrated luminosity, ranges between $0.5 < \kappa_\lambda < 1.6$ at the 1σ level and $0 < \kappa_\lambda < 2.5$ at the 2σ level. This sensitivity is based on a combination of the $b\bar{b}b\bar{b}$,

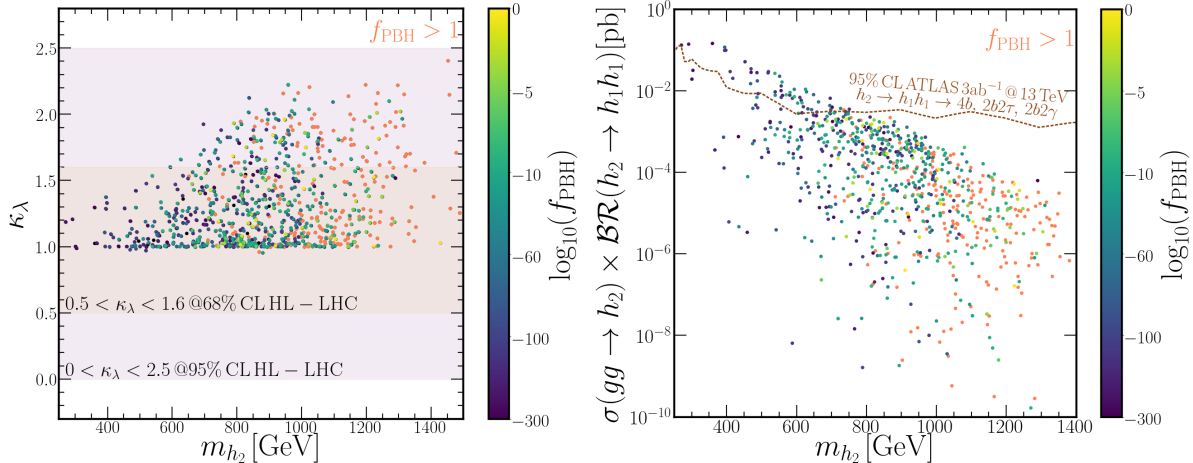


FIG. 11: Left panel: The mass of the heavy scalar m_{h_2} versus the triple Higgs coupling modifier $\kappa_\lambda = \lambda_{111}/\lambda_{111}^{\text{SM}}$. The dashed curve represents the projected sensitivity at the HL-LHC with an integrated luminosity of 3 ab^{-1} , shown at the 1σ and 2σ levels [99]. Right panel: The HL-LHC projected limits for the cross-section of the heavy Higgs decaying into di-Higgs, $h_2 \rightarrow h_1 h_1$, are represented by the dashed curve [100]. The points are color-coded by f_{PBH} , and the orange color denotes the parameter excluded from DM overproduction $f_{\text{PBH}} > 1$.

$b\bar{b}\gamma\gamma$, and $b\bar{b}\tau^+\tau^-$ channels [99]. Notably, for the PBH formation parameter space, κ_λ tends to exceed the unity. This is evident when expanding the coupling λ_{111} in Eq. (12), using a Taylor series for small values of θ [36],

$$\lambda_{111} = \frac{m_{h_1}^2}{2v_{\text{EW}}} \left[1 + \theta^2 \left(-\frac{3}{2} + \frac{2m_{h_2}^2 - 2b_3 v_s - 4b_4 v_s^2}{m_{h_1}^2} \right) + \mathcal{O}(\theta^3) \right]. \quad (37)$$

The preference for negative values of the cubic coupling b_3 and a tendency towards $\Theta_{hs}^{-1} \sim -0.55$ ensure that $\kappa_\lambda \gtrsim 1$. The HL-LHC will be sensitive, at the one to two σ level, to a substantial fraction of the parameter points that allow for PBH formation, using the triple Higgs coupling constraints.

Resonant di-Higgs searches also provide relevant probes for parameter space regime that favors PBHs. In the right panel of Fig. 11, we present the heavy Higgs cross section decaying to di-Higgs, $h_2 \rightarrow h_1 h_1$, as a function of heavy Higgs mass m_{h_2} . The ATLAS collaboration obtained the 95% confidence level limit for this channel by combining the final states $4b$, $2b2\tau$, and $2b2\gamma$ in Ref. [100]. The dotted line represents this result scaled to the high-luminosity LHC with $\mathcal{L} = 3 \text{ ab}^{-1}$ of data. The signal cross-section for Higgs production was obtained at NNLO+NNLL QCD and incorporates the effects of top and bottom quark masses up to NLO [42, 101, 102]. The resonant di-Higgs channel can probe some of the parameter space that displays PBH formation with $m_{h_2} < 800 \text{ GeV}$ with relatively low PBH fraction.

The resonant di-boson ZZ/WW searches can also lead to relevant constraints. In Fig. 12, we present the sensitivity to the PBH parameter space from the di-boson channels $h_2 \rightarrow ZZ$ (left panel) and $h_2 \rightarrow WW$ (right panel). In Refs. [103, 104], the ATLAS and CMS collaborations analyzed the projected sensitivities of the HL-LHC to heavy Higgs resonant searches in the channels $pp \rightarrow h_2 \rightarrow ZZ \rightarrow 2\ell 2q$ at $\sqrt{s} = 13 \text{ TeV}$ and $pp \rightarrow h_2 \rightarrow WW \rightarrow \ell\nu 2q$ at $\sqrt{s} = 14 \text{ TeV}$. The results are depicted as dotted lines in Fig. 12. While the $h_2 \rightarrow WW$ channel lacks the sensitivity to probe the PBH formation parameter space, the $h_2 \rightarrow ZZ$ channel offers significant sensitivity to PBH formation parameter space at HL-LHC with $m_{h_2} \lesssim 900 \text{ GeV}$.

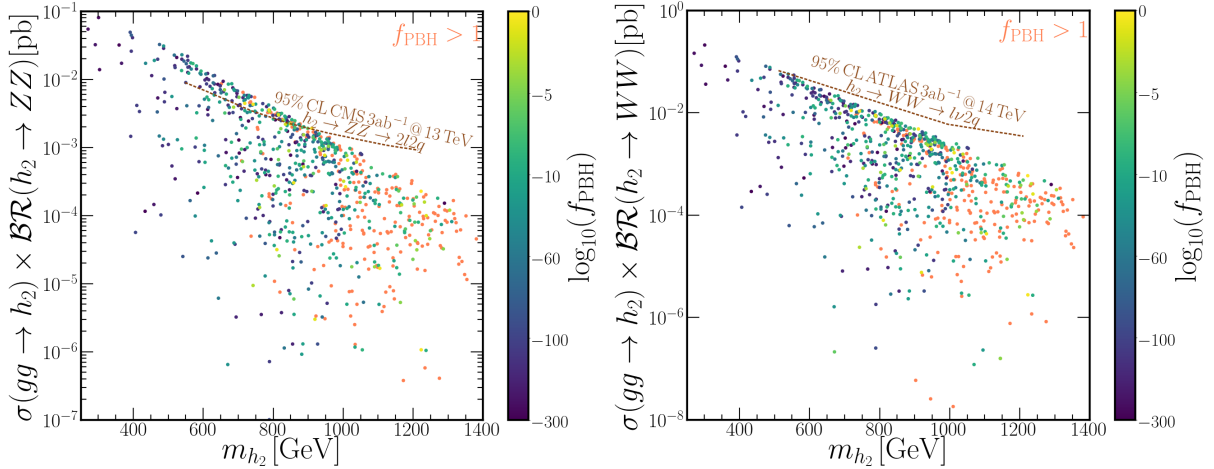


FIG. 12: The mass of the heavy scalar m_{h_2} versus , di-boson $h_2 \rightarrow ZZ$ (left panel) and $h_2 \rightarrow WW$ (right panel) color coded by f_{PBH} and, the orange color denotes the parameter excluded due to overproduction of DM $f_{\text{PBH}} > 1$. The dashed lines in the figure represent the HL-LHC sensitivity projections from ATLAS and CMS collaborations [103, 104].

VI. CONCLUSION

In this paper, we considered the PBH formation during the electroweak phase transition in the singlet extension of the SM, xSM. PBH formation during phase transition requires sufficient supercooling such that the probability of having a *late patch*, where the system remains in the false vacuum, is large. In order to achieve that, it is found that the S_3/T behavior as a function of temperature should have a U-shape, which provides a strict requirement on the evolution of the potential. By scrutinizing the evolution of the barrier and depth of the true vacuum, we find a strong correlation between the shape of the effective potential with the PBH formation. Further, such correlation also provides a hint about the preferred parameter space for the PBH formation through the relative relation between the barrier and the depth of the electroweak vacuum.

PBHs, which can serve as dark matter components [75], can leave observable signals in microlensing experiments due to their gravitational effects. The mass of these PBHs is restricted to a narrow range, approximately 10^{-5} solar mass, which is about the mass of Earth. This constraint is influenced by the scale of the electroweak phase transition in the xSM. Furthermore, our analysis shows that this model can produce a broad spectrum of dark matter fractions. Notably, the current OGLE experiment has observed six ultra-

short timescale events consistent with Earth-mass PBHs. Hence, PBH formation through supercooled electroweak phase transition provides a promising explanation.

Additionally, we find that the peak frequency of the gravitational wave induced by such a supercooled phase transition can be naturally probed by the future LISA mission with sufficient signal strength because of its supercooled nature. LISA’s potential to probe the PBH formation in the xSM model positions it to either confirm the proposed PBH scenario or definitively refute it down to extremely small values of total dark matter fraction made of PBHs, $f_{\text{PBH}} > 10-300$.

The formation of PBHs imposes stringent constraints on the parameter space of xSM model, particularly concerning the cubic terms that induce the barrier in the effective potential. Collider searches emerge as valuable tools for investigating these regions, capable of encompassing significant portions of the parameter space, even with low PBH fractions f_{PBH} . Furthermore, collider searches have the potential to scrutinize the model in the event of PBH discovery. Therefore, there is strong complementarity in probing PBHs through the combined use of collider searches, microlensing observations, and gravitational wave experiments.

Acknowledgments

We would like to thank Iason Baldes, Sumit Biswas, Bhaskar Dutta, Shinya Kanemura, Ian Lewis, Philip Lu, María Olalla Olea-Romacho, Masanori Tanaka, Ke-Pan Xie, and Tao Xu for helpful discussions. D.G. thanks the group at the IPPP-Durham University for hosting him during the final stages of this project. D.G. and A.K. are supported by the U.S. Department of Energy under grant number DE-SC 0016013. Y.W. is supported by the National Natural Science Foundation of China (NNSFC) under grant No. 12305112. Some computing for this project was performed at the High Performance Computing Center at Oklahoma State University, supported in part through the National Science Foundation grant OAC-1531128.

Appendix A: Parametrization scan for xSM

This appendix illustrates how we scan the xSM scalar potential parameter space, satisfying current phenomenological constraints. The scalar potential in Eq.(1) can be expressed differently, where EW vacuum has VEV $\langle S \rangle = 0$ by translating the coordinate system [105, 106]. In this basis, scalar potential has an additional contribution of tadpole term $b'_1 S$,

$$V(H, S) = -\mu'^2 H^\dagger H + \lambda'(H^\dagger H)^2 + \frac{a'_1}{2} H^\dagger H S + \frac{a'_2}{2} H^\dagger H S^2 + b'_1 S + \frac{b'_2}{2} S^2 + \frac{b'_3}{3} S^3 + \frac{b'_4}{4} S^4, \quad (\text{A1})$$

The minimization condition at EW vacuum $(v_{\text{EW}}, 0)$ provides,

$$\mu'^2 = \lambda' v_{\text{EW}}^2 \quad b'_1 = -\frac{v_{\text{EW}}^2}{4} a'_1, \quad (\text{A2})$$

and the remaining coefficients can be expressed in terms of the scalar masses and mixing angle,

$$a'_1 = \frac{s_{2\theta}}{v_{\text{EW}}} (m_{h_1}^2 - m_{h_2}^2), \quad b'_2 + \frac{a'_2}{2} v_{\text{EW}}^2 = m_{h_1}^2 s_\theta^2 + m_{h_2}^2 c_\theta^2, \quad \lambda' = \frac{1}{2v_{\text{EW}}^2} (m_{h_1}^2 c_\theta^2 + m_{h_2}^2 s_\theta^2). \quad (\text{A3})$$

Consequently, we can use the following parameters as input parameters

$$\{m_{h_2}, \theta, a'_2, b'_3, b'_4\}. \quad (\text{A4})$$

We conducted a random uniform scan over the parameter region,

$$\begin{aligned} m_{h_2} &\in (130, 1500) \text{ GeV}, & \theta &\in (-0.35, 0.35), & \frac{b'_3}{v_{\text{EW}}} &\in (-4\pi, 4\pi), \\ b'_4 &\in (0.001, \frac{4\pi}{3}), & a'_2 &\in (-2\sqrt{\lambda' b'_4}, 4\pi). \end{aligned} \quad (\text{A5})$$

To obtain scalar potential in the form of Eq.(1), we shift $s \rightarrow s + \sigma$ and the coefficients transforms as

$$\mu^2 = \mu'^2 - \frac{1}{2} a'_2 \sigma^2 - \frac{1}{2} a'_1 \sigma, \quad (\text{A6})$$

$$a_1 = a'_1 + 2a'_2 \sigma, \quad (\text{A7})$$

$$b_1 = b'_1 + b'_4 \sigma^3 + b'_3 \sigma^2 + b'_2 \sigma, \quad (\text{A8})$$

$$b_2 = b'_2 + 3b'_4 \sigma^2 + 2b'_3 \sigma, \quad (\text{A9})$$

$$b_3 = b'_3 + 3b'_4\sigma. \quad (\text{A10})$$

The coefficients a_2 , λ , and b_4 remain the same as their counterparts and we obtain σ such that $b_1 = 0$. The shifted s obtains a VEV $v_s = -\sigma$. If v_s is negative, we can ensure that v_s remains positive by the Z_2 transformation $v_s \rightarrow -v_s$, $s \rightarrow -s$, $a_1 \rightarrow -a_1$ and $b_3 \rightarrow -b_3$.

Appendix B: Phenomenological constraints

In this appendix, we present the theoretical and experimental constraints used in this analysis [32, 34, 40, 107–109].

- **Boundedness condition:** The scalar potential in Eq. (1) must be bounded below.

Demanding this for arbitrary field directions provides the condition [105]

$$\lambda > 0, \quad b_4 > 0, \quad a_2 > -\sqrt{4\lambda b_4}. \quad (\text{B1})$$

- **EW vacuum stability:** To guarantee that the EW vacuum is stable at zero temperature, one should ensure that no deeper minimum exists in the potential. We determine the nature of each minimum by solving $\partial V/\partial\phi_i = 0$, $\{\phi_1 = h, \phi_2 = s\}$ and evaluating the eigenvalues of the Hessian matrix $\partial^2 V/\partial\phi_i\phi_j$.
- **Perturbative unitarity:** Perturbative unitarity constraints the behavior of particle scatterings at high energies. At tree level, it requires all partial wave amplitudes $a_\ell(s)$ for all $2 \rightarrow 2$ scattering processes to satisfy $\text{Re } a_\ell(s) \leq \frac{1}{2}$ for $\sqrt{s} \rightarrow \infty$ [110]. Here, we include all scalar/vector boson $2 \rightarrow 2$ scattering channels at the leading order. The details of the evaluation of the S-matrix are provided in Appendix C.
- **Higgs signal strength measurements:** The 125 GeV Higgs signal measurements in various production and decay channels require the couplings of h_1 to be close to the SM Higgs. In this analysis, we use HiggsSignals [111, 112]⁸ to apply the Higgs coupling constraints from ATLAS and CMS.
- **Heavy Higgs searches:** The heavy SM-like Higgs boson searches in ATLAS and CMS can provide a probe for h_2 [114–121]. The partial decay width of heavy Higgs

⁸ We used HiggsTools [113] to perform the HiggsBounds and HiggsSignals analysis in the singlet framework.

scalar decay into SM particles is given by

$$\Gamma_{h_2 \rightarrow \text{SM}} = s_\theta^2 \Gamma^{\text{SM}}(m_{h_2}), \quad (\text{B2})$$

where $\Gamma^{\text{SM}}(m_{h_2})$ is the SM Higgs decay width evaluated at $m_{h_2} < 2m_{h_1}$ [122]. In the regime $m_{h_2} > 2m_{h_1}$, the decay mode $h_2 \rightarrow h_1 h_1$ is kinematically allowed. The corresponding partial decay width is given by [32, 33]

$$\Gamma_{h_2 \rightarrow h_1 h_1} = \frac{\lambda_{211}^2 \sqrt{1 - \frac{4m_{h_1}^2}{m_{h_2}^2}}}{8\pi m_{h_2}}. \quad (\text{B3})$$

We used HiggsBounds [123–126] to implement the current experimental constraints.

- **Electroweak precision measurements:** The W boson mass measurement [127] and oblique EW corrections [128, 129] put additional constraints on the parameter space of the xSM. The W boson mass m_W depends on the loop corrections of the vector boson self-energies [127]. In the xSM model, the reduced Higgs coupling and the presence of heavier scalar can modify the loop corrections, and these modifications only depend on two parameters θ and m_{h_2} . The same parameters enter the corrections to the oblique parameters S , T , and U . The W mass experimental value $m_W^{\text{exp}} = 80.3545 \pm 0.0059 \text{ GeV}$ [130] puts a more stringent bound on these parameters than the oblique corrections [32, 127].

Appendix C: Perturbative unitarity of the S-matrix

For scalars (and longitudinal gauge boson) $2 \rightarrow 2$ process, the scattering amplitude can be written as

$$A(\alpha) = 16\pi \sum_J (2J+1) a_J P_J(\cos \alpha), \quad (\text{C1})$$

where α denotes scattering angle and P_J is the Legendre polynomial. The perturbative unitarity demands $|Re(a_0^{\text{max}})| \leq \frac{1}{2}$ [131]. There are seven neutral ($h_1 h_1$, $h_2 h_2$, $h_1 h_2$, $h_1 Z$, $h_2 Z$, ZZ , $W^+ W^-$), three singly-charged ($h_1 W^+$, $h_2 W^+$, $Z W^+$) and one doubly-charged ($W^+ W^+$) channels. Therefore, the scattering amplitude matrix a_0 can be written as a direct sum of matrices $a_0 = \mathcal{S}_1 \bigoplus \mathcal{S}_2 \bigoplus \mathcal{S}_3$ from these three groups [36]. The perturbative unitarity condition translates into the magnitude of the largest eigenvalue should be less than 8π .

The non-zero elements of the neutral 7×7 submatrix \mathcal{S}_1 are given by [36, 132]

$$\mathcal{S}_{11} = -3(a_2 c_\theta^2 s_\theta^2 + b_4 s_\theta^4 + \lambda c_\theta^4), \quad (\text{C2})$$

$$\mathcal{S}_{12} = \frac{1}{8}(3c_{4\theta}(-a_2 + b_4 + \lambda) - a_2 - 3b_4 - 3\lambda), \quad (\text{C3})$$

$$\mathcal{S}_{13} = \frac{3s_{2\theta}(c_{2\theta}(-a_2 + b_4 + \lambda) - b_4 + \lambda)}{2\sqrt{2}}, \quad (\text{C4})$$

$$\mathcal{S}_{16} = -\frac{1}{2}a_2 s_\theta^2 - \lambda c_\theta^2, \quad (\text{C5})$$

$$\mathcal{S}_{17} = -\frac{a_2 s_\theta^2 + 2\lambda c_\theta^2}{\sqrt{2}}, \quad (\text{C6})$$

$$\mathcal{S}_{22} = -3(a_2 c_\theta^2 s_\theta^2 + b_4 c_\theta^4 + \lambda s_\theta^4), \quad (\text{C7})$$

$$\mathcal{S}_{23} = -\frac{3s_{2\theta}(c_{2\theta}(-a_2 + b_4 + \lambda) + b_4 - \lambda)}{2\sqrt{2}}, \quad (\text{C8})$$

$$\mathcal{S}_{26} = -\frac{1}{2}a_2 c_\theta^2 - \lambda s_\theta^2, \quad (\text{C9})$$

$$\mathcal{S}_{27} = -\frac{a_2 c_\theta^2 + 2\lambda s_\theta^2}{\sqrt{2}}, \quad (\text{C10})$$

$$\mathcal{S}_{33} = \frac{1}{4}(3c_{4\theta}(-a_2 + b_4 + \lambda) - a_2 - 3b_4 - 3\lambda), \quad (\text{C11})$$

$$\mathcal{S}_{36} = \frac{(2\lambda - a_2)c_\theta s_\theta}{\sqrt{2}}, \quad (\text{C12})$$

$$\mathcal{S}_{37} = (2\lambda - a_2)c_\theta s_\theta, \quad (\text{C13})$$

$$\mathcal{S}_{44} = -a_2 s_\theta^2 - 2\lambda c_\theta^2, \quad (\text{C14})$$

$$\mathcal{S}_{45} = (2\lambda - a_2)c_\theta s_\theta, \quad (\text{C15})$$

$$\mathcal{S}_{55} = -a_2 c_\theta^2 - 2\lambda s_\theta^2, \quad (\text{C16})$$

$$\mathcal{S}_{66} = -3\lambda, \quad (\text{C17})$$

$$\mathcal{S}_{67} = -\sqrt{2}\lambda, \quad (\text{C18})$$

$$\mathcal{S}_{77} = -4\lambda. \quad (\text{C19})$$

For singly-charged channel the submatrix \mathcal{S}_2 is given by

$$\mathcal{S}_2 = \begin{bmatrix} -2\lambda c_\theta^2 - a_2 s_\theta^2 & (2\lambda - 2)c_\theta s_\theta & 0 \\ (2\lambda - 2)c_\theta s_\theta & -a_2 c_\theta^2 - 2\lambda s_\theta^2 & 0 \\ 0 & 0 & -2\lambda \end{bmatrix}. \quad (\text{C20})$$

We have only one process for the doubly-charged channel and the submatrix is $\mathcal{S}_3 = -2\lambda$.

Appendix D: PBH calculation

In the following discussion, it is implied that quantities without specific indices are defined within the context of the false vacuum. Using $dt = -\frac{dT}{HT}$, we can express Eq. (28) in terms of temperature as [23, 70]

$$F_{\text{in}}(T) = \exp \left[-\frac{4\pi}{3} \int_T^{T_i} \frac{dT' \Gamma(T')}{T'^4 H(T')^3} \left(\int_T^{T'} \frac{A_{\text{in}}(T', \tilde{T}) d\tilde{T}}{H(\tilde{T})} \right)^3 \right], \quad (\text{D1})$$

where H is the Hubble rate at false vacuum H_{false} and we define T as the temperature of the false vacuum. The Hubble rate at the false vacuum is obtained from the Friedmann equation including the vacuum and radiation energy inside the false vacuum:

$$H(T)^2 \equiv H_{\text{false}}(T)^2 = \frac{1}{3M_{\text{Pl}}^2} \left(\Lambda_{\text{vac}}(T) + \frac{\pi^2}{30} g_{\star} T^4 \right). \quad (\text{D2})$$

Furthermore, the function $A_{\text{in}}(T', \tilde{T})$ in Eq. (D1) is defined as

$$A_{\text{in}}(T', \tilde{T}) = \frac{a_{\text{in}}(T') T'}{a_{\text{in}}(\tilde{T}) \tilde{T}}. \quad (\text{D3})$$

The Friedman equation governing the evolution of Hubble rate, radiation energy density, vacuum energy density, and scale factor of the *late patch* can be rewritten as a function of the temperature as

$$H_{\text{in}}^2 = \frac{1}{3M_{\text{Pl}}^2} \left(\rho_R^{\text{in}} + \rho_V^{\text{in}} \right), \quad (\text{D4a})$$

$$\frac{d\rho_R^{\text{in}}}{dT} = \frac{4H_{\text{in}}\rho_R^{\text{in}}}{HT} - \frac{d\rho_V^{\text{in}}}{dT}, \quad (\text{D4b})$$

$$\frac{da_{\text{in}}}{dT} = -\frac{a_{\text{in}}}{T} \frac{H_{\text{in}}}{H}, \quad (\text{D4c})$$

where vacuum energy density is given by $\rho_V^{\text{in}} = F_{\text{in}}(T) \Lambda_{\text{vac}}(T)$. The temperature evolution of ρ^{in} , the scalar factor a_{in} for this region can be solved numerically using Eq. (D4) with initial conditions of the false vacuum which are given by

$$\rho_V^{\text{in}}(T_i) = \Lambda_{\text{vac}}(T_i), \quad \rho_R^{\text{in}}(T_i) = \frac{\pi^2}{30} g_{\star} T_i^4, \quad a_{\text{in}}(T_i) = \frac{1}{T_i}. \quad (\text{D5})$$

In a similar approach, we can consider the evolution of the *background region*, where we can assume for the surrounding region that the first bubble nucleates around critical temperature

T_c , and the average spatial fraction of the false vacuum in such *background region* is given by ⁹

$$F_{\text{out}}(T) = \exp \left[-\frac{4\pi}{3} \int_T^{T_c} \frac{dT' \Gamma(T')}{T'^4 H(T')^3} \left(\int_T^{T'} \frac{A_{\text{out}}(T', \tilde{T}) d\tilde{T}}{H(\tilde{T})} \right)^3 \right], \quad (\text{D6})$$

where the function $A_{\text{out}}(T', \tilde{T})$ is defined similar to Eq. (D3) by replacing a_{in} with a_{out} and all quantities without specific indices are defined at false vacuum. The evolution of Hubble rate, scale factor, radiation energy density and vacuum energy density of the *background region* can be solved numerically using a similar equation of Eq. (D4), by substituting indices from “in” to “out” and with the initial condition given by

$$\rho_V^{\text{out}}(T_c) = \Lambda_{\text{vac}}(T_c), \quad \rho_{\text{rad}}^{\text{out}}(T_c) = \frac{\pi^2}{30} g_{\star} T_c^4, \quad a_{\text{out}}(T_c) = \frac{1}{T_c}. \quad (\text{D7})$$

The probability that no bubble nucleates in the past wall cone of the Hubble volume at $T > T_i$ is given by [17, 20, 23],

$$P(T_i) = \exp \left[- \int_{T_i}^{T_c} \frac{dT' \Gamma(T')}{T' H(T')^3} a_{\text{in}}(T')^3 V_{\text{coll}} \right], \quad (\text{D8})$$

where the volume factor V_{coll} is given by

$$V_{\text{coll}} = \frac{4\pi}{3} \left[\frac{1}{a_{\text{in}}(T_{\text{PBH}}) H_{\text{in}}(T_{\text{PBH}})} + \int_{T_{\text{PBH}}}^{T'} \frac{d\tilde{T}}{\tilde{T} H(\tilde{T}) a_{\text{out}}(\tilde{T})} \right]^3. \quad (\text{D9})$$

Appendix E: Gravitational wave signatures

First-order phase transition (FOPT) occurring in the early Universe may lead to detectable stochastic gravitational wave (GW) signals in the present era [96, 133, 134]. Supercooling is anticipated for the parameter space, leading to PBH formation. Therefore, we designate the percolation temperature T_p as the phase transition temperature, which serves as the point for evaluating gravitational waves. During FOPT, GWs emerge from three distinct sources: bubble collisions, sound waves, and magnetohydrodynamic (MHD) turbulence. The GW spectrum, denoted as $\Omega_{\text{GW}}(f)$, represents the current GW energy density per logarithmic frequency interval relative to the critical energy density of the Universe. Thus, $\int \Omega_{\text{GW}} d\ln f$ signifies the fraction of GW energy density compared to the critical

⁹ The critical temperature T_c is defined as the point at which the false and would-be true vacua degenerate.

energy density of the Universe. The GW energy density can be linearly approximated as

$$\Omega_{\text{GW}} h^2 = \Omega_{\text{coll}} h^2 + \Omega_{\text{SW}} h^2 + \Omega_{\text{turb}} h^2. \quad (\text{E1})$$

Here, $h = H_0/100 \text{ Km/s/Mpc}$ represents the dimensionless Hubble parameter at the present time. Next, we will examine each of the components in Eq. (E1).

1. Sound waves

The energy released during the phase transition to the plasma can be distributed between heat and fluid motion. Numerical estimations suggest that the energy-momentum tensor of the fluid following bubble collision bears resemblance to that of an ensemble of sound waves [135–137]. Notably, these sound waves emerge as a significant source of gravitational waves. The redshifted peak amplitude of the gravitational waves stemming from these sound waves are given by [64, 136],

$$h^2 \Omega_{\text{sw}} = 3 \mathcal{R}_\Omega \left(\frac{k_s \alpha}{\alpha + 1} \right)^2 \left(\frac{H_\star R_\star}{c_{s,f}} \right) \frac{M(s, r_b, b)}{\mu_f(r_b)} \Upsilon(\tau_{\text{sw}}) \tilde{\Omega}_{\text{GW}}, \quad (\text{E2})$$

where the redshift factor for the amplitude \mathcal{R}_Ω is provided by, [64]

$$R_\Omega = 1.384 \times 10^{33} \left(\frac{\text{GeV}^3}{s_1} \right)^{\frac{4}{3}} \left(\frac{H_\star}{\text{Gev}} \right)^2, \quad (\text{E3})$$

where s_1 is the entropy at reheat temperature T_{rh} and H_\star is the Hubble factor at gravitational wave temperature T_p . The reheating temperature can be approximated as,

$$T_{\text{rh}} = (1 + \alpha)^{\frac{1}{4}} T_p. \quad (\text{E4})$$

To estimate mean bubble separation R_\star , we calculate the mean bubble number density considering that true vacuum bubbles can only nucleate within regions that remain in the false vacuum state. The mean bubble separation R_\star is given by [63, 138],

$$R_\star(T) \equiv (n_B(T))^{-\frac{1}{3}} = \left(\int_T^{T_c} dT' \frac{\Gamma(T') F_{\text{out}}(T')}{T' H(T')} \left(\frac{a_{\text{out}}(T')}{a_{\text{out}}(T)} \right)^3 \right)^{-\frac{1}{3}}. \quad (\text{E5})$$

The spectral shape $M(s, r_b, b)$ is provided by [64, 136],

$$M(s, r_b, b) = s^9 \left(\frac{1 + r_b^4}{r_b^4 + s^4} \right)^{\frac{9-b}{b}} \left(\frac{b+4}{b+4-m+m^2} \right)^{\frac{b+4}{2}}, \quad (\text{E6})$$

where,

$$m = (9r_b^4 + b) / (r_b^4 + 1), \quad (\text{E7})$$

$$s = f/f_p, \quad (\text{E8})$$

$$r_b = f_b/f_p, \quad (\text{E9})$$

$$\mu_f(r_b) = 4.78 - 6.27r_b + 3.34r_b^2. \quad (\text{E10})$$

In accordance with Table IV of [136], we use $b = 1$ and $\tilde{\Omega}_{\text{GW}} = 0.01$. The f_b and f_p denote the redshifted frequencies corresponding to mean bubble separation and fluid shell thickness, which breaks power laws and are given by,

$$f_b = 1.58\mathcal{R}_f \left(\frac{1}{R_\star} \right) \left(\frac{z_p}{10} \right) \quad (\text{E11})$$

$$f_p = 1.58\mathcal{R}_f \left(\frac{1}{R_\star \Delta_w} \right) \left(\frac{z_p}{10} \right), \quad (\text{E12})$$

where $\Delta_w \approx |v_w - c_{s,f}| / v_w$ captures fluid shell thickness and \mathcal{R}_f incorporates the redshift factor of the frequency,

$$\mathcal{R}_f = 4.280 \times 10^{11} \frac{\text{Hz}}{\text{Gev}} \left(\frac{1\text{GeV}^3}{s_1} \right)^{\frac{1}{3}}. \quad (\text{E13})$$

We approximate speed of sound at false vacuum $c_{s,f} \approx 1/\sqrt{3}$ [63] and v_w is the Chapman-Jouguet velocity [67, 68],

$$v_w = \frac{1 + \sqrt{3\alpha(1 + c_{s,f}^2(3\alpha - 1))}}{c_{s,f}^{-1} + 3\alpha c_{s,f}}. \quad (\text{E14})$$

We consider the dimensionless wave number at the peak to be $z_p = 10$, a value applicable to the supersonic detonations we are considering [136, 139]. The efficiency factor for the sound wave spectrum k_s is provided by [96]

$$k_s = \frac{\alpha}{0.73 + 0.083\sqrt{\alpha} + \alpha}. \quad (\text{E15})$$

Recent studies [140, 141] demonstrate a suppression factor $\Upsilon(\tau_{\text{SW}})$ arising from the finite active period τ_{SW} of sound waves

$$\Upsilon(\tau_{\text{SW}}) = 1 - \frac{1}{\sqrt{1 + 2\tau_{\text{SW}}H_\star}}, \quad (\text{E16})$$

where duration $\tau_{\text{SW}} = R_\star/\bar{U}_f$ and represents the mean square velocity [142]

$$\bar{U}_f^2 = \frac{3}{4} \frac{\alpha}{1 + \alpha} k_s. \quad (\text{E17})$$

2. Bubble collisions

Nucleated bubbles, upon collision, lose their spherical symmetry, leading to the production of gravitational waves [143, 144]. The redshifted peak amplitude due to bubble collisions is given by [64, 145],

$$\Omega_{\text{coll}} = \mathcal{R}_\Omega A \left(\frac{H_\star R_\star}{(8\pi)^{\frac{1}{3}} v_w} \right)^2 \left(\frac{k_c \alpha}{1 + \alpha} \right)^2 S_{\text{coll}}(f), \quad (\text{E18})$$

where the spectral shape is provided by,

$$S_{\text{coll}} = \frac{(a + b)^c}{\left[b \left(\frac{f}{f_{\text{coll}}} \right)^{-\frac{a}{c}} + a \left(\frac{f}{f_{\text{coll}}} \right)^{\frac{b}{c}} \right]^c}. \quad (\text{E19})$$

For the scenario where $T_{\tau\tau} \propto R^{-3}$, the fitting parameters A , a , b , and c are available in Table I of Ref. [145]. The redshifted peak frequency is given by,

$$f_{\text{coll}} = \mathcal{R}_f \left(\frac{0.77(8\pi)^{\frac{1}{3}} v_w}{2\pi R_\star} \right) \quad (\text{E20})$$

3. MHD turbulence

The energy injected into the plasma can trigger turbulence in the fluid, particularly in scenarios where the early Universe plasma exhibits an extremely high Reynolds number [146]. This turbulent motion can be a significant source of gravitational waves [147]. Moreover, turbulent motion within a fully ionized plasma can generate a turbulent magnetic field, further contributing to the production of gravitational waves. The redshifted peak amplitude stemming from turbulence can be parametrized by [148, 149]

$$\Omega_{\text{turb}}(f) = 9.0 \mathcal{R}_\Omega H_\star R_\star \left(\frac{k_{\text{turb}} \alpha}{1 + \alpha} \right)^2 S_{\text{turb}}(f), \quad (\text{E21})$$

where based on numerical simulation we adopt $k_{\text{turb}} = 0.05 k_s$ [96] and the unnormalized spectral shape is given by

$$S_{\text{turb}}(f) = \frac{(f/f_{\text{turb}})^3}{(1 + f/f_{\text{turb}})^{\frac{11}{3}} (1 + 8\pi f / (\mathcal{R}_\star H_\star))}, \quad (\text{E22})$$

where $f_{\text{turb}} = \mathcal{R}_f \frac{3.5}{R_*}$ is the redshifted peak frequency [149].

- [1] S. Hawking, *Gravitationally collapsed objects of very low mass*, *Mon. Not. Roy. Astron. Soc.* **152** (1971) 75.
- [2] B. J. Carr and S. W. Hawking, *Black holes in the early Universe*, *Mon. Not. Roy. Astron. Soc.* **168** (1974) 399–415.
- [3] B. J. Carr, *The primordial black hole mass spectrum.*, *Astrophys. J.* **201** (Oct., 1975) 1–19.
- [4] M. Y. Khlopov, R. V. Konoplich, S. G. Rubin and A. S. Sakharov, *Formation of black holes in first order phase transitions*, [hep-ph/9807343](https://arxiv.org/abs/hep-ph/9807343).
- [5] J. B. Dent, B. Dutta and T. Xu, *Multi-messenger Probes of Asteroid Mass Primordial Black Holes: Superradiance Spectroscopy, Hawking Radiation, and Microlensing*, [2404.02956](https://arxiv.org/abs/2404.02956).
- [6] E. Bertuzzo, Y. F. Perez-Gonzalez, G. M. Salla and R. Z. Funchal, *Gravitationally produced Dark Matter and primordial black holes*, [2405.17611](https://arxiv.org/abs/2405.17611).
- [7] S. W. Hawking, I. G. Moss and J. M. Stewart, *Bubble collisions in the very early universe*, *Phys. Rev. D* **26** (Nov, 1982) 2681–2693.
- [8] I. G. Moss, *Singularity formation from colliding bubbles*, *Phys. Rev. D* **50** (Jul, 1994) 676–681.
- [9] M. Lewicki and V. Vaskonen, *On bubble collisions in strongly supercooled phase transitions*, *Phys. Dark Univ.* **30** (2020) 100672, [[1912.00997](https://arxiv.org/abs/1912.00997)].
- [10] M. J. Baker, M. Breitbach, J. Kopp and L. Mittnacht, *Primordial Black Holes from First-Order Cosmological Phase Transitions*, [2105.07481](https://arxiv.org/abs/2105.07481).
- [11] M. J. Baker, M. Breitbach, J. Kopp and L. Mittnacht, *Detailed Calculation of Primordial Black Hole Formation During First-Order Cosmological Phase Transitions*, [2110.00005](https://arxiv.org/abs/2110.00005).
- [12] P. Huang and K.-P. Xie, *Leptogenesis triggered by a first-order phase transition*, *JHEP* **09** (2022) 052, [[2206.04691](https://arxiv.org/abs/2206.04691)].
- [13] P. Huang and K.-P. Xie, *Primordial black holes from an electroweak phase transition*, *Phys. Rev. D* **105** (2022) 115033, [[2201.07243](https://arxiv.org/abs/2201.07243)].
- [14] T. C. Gehrman, B. Shams Es Haghi, K. Sinha and T. Xu, *The primordial black holes that disappeared: connections to dark matter and MHz-GHz gravitational Waves*, *JCAP* **10** (2023) 001, [[2304.09194](https://arxiv.org/abs/2304.09194)].

[15] M. Lewicki, K. Müürsepp, J. Pata, M. Vasar, V. Vaskonen and H. Veermäe, *Dynamics of false vacuum bubbles with trapped particles*, *Phys. Rev. D* **108** (2023) 036023, [2305.07702].

[16] H. Kodama, M. Sasaki and K. Sato, *Abundance of Primordial Holes Produced by Cosmological First-Order Phase Transition*, *Progress of Theoretical Physics* **68** (12, 1982) 1979–1998,
[\[https://academic.oup.com/ptp/article-pdf/68/6/1979/5311817/68-6-1979.pdf\]](https://academic.oup.com/ptp/article-pdf/68/6/1979/5311817/68-6-1979.pdf).

[17] J. Liu, L. Bian, R.-G. Cai, Z.-K. Guo and S.-J. Wang, *Primordial black hole production during first-order phase transitions*, *Phys. Rev. D* **105** (2022) L021303, [2106.05637].

[18] K. Hashino, S. Kanemura and T. Takahashi, *Primordial black holes as a probe of strongly first-order electroweak phase transition*, *Phys. Lett. B* **833** (2022) 137261, [2111.13099].

[19] K. Hashino, S. Kanemura, T. Takahashi and M. Tanaka, *Probing first-order electroweak phase transition via primordial black holes in the effective field theory*, *Phys. Lett. B* **838** (2023) 137688, [2211.16225].

[20] K. Kawana, T. Kim and P. Lu, *PBH Formation from Overdensities in Delayed Vacuum Transitions*, 2212.14037.

[21] M. Lewicki, P. Toczek and V. Vaskonen, *Primordial black holes from strong first-order phase transitions*, *JHEP* **09** (2023) 092, [2305.04924].

[22] Y. Gouttenoire and T. Volansky, *Primordial Black Holes from Supercooled Phase Transitions*, 2305.04942.

[23] I. Baldes and M. O. Olea-Romacho, *Primordial black holes as dark matter: Interferometric tests of phase transition origin*, 2307.11639.

[24] A. Salvio, *Supercooling in radiative symmetry breaking: theory extensions, gravitational wave detection and primordial black holes*, *JCAP* **12** (2023) 046, [2307.04694].

[25] A. Conaci, L. Delle Rose, P. S. B. Dev and A. Ghoshal, *Slaying Axion-Like Particles via Gravitational Waves and Primordial Black Holes from Supercooled Phase Transition*, 2401.09411.

[26] M. M. Flores, A. Kusenko and M. Sasaki, *Revisiting formation of primordial black holes in a supercooled first-order phase transition*, 2402.13341.

[27] M. Lewicki, P. Toczek and V. Vaskonen, *Black holes and gravitational waves from slow phase transitions*, 2402.04158.

[28] S. Kanemura, M. Tanaka and K.-P. Xie, *Primordial black holes from slow phase transitions*:

a model-building perspective, 2404.00646.

- [29] H. Niikura, M. Takada, S. Yokoyama, T. Sumi and S. Masaki, *Constraints on Earth-mass primordial black holes from OGLE 5-year microlensing events*, *Phys. Rev. D* **99** (2019) 083503, [1901.07120].
- [30] J. Scholtz and J. Unwin, *What if Planet 9 is a Primordial Black Hole?*, *Phys. Rev. Lett.* **125** (2020) 051103, [1909.11090].
- [31] S. Profumo, M. J. Ramsey-Musolf and G. Shaughnessy, *Singlet Higgs phenomenology and the electroweak phase transition*, *JHEP* **08** (2007) 010, [0705.2425].
- [32] T. Robens and T. Stefański, *Status of the Higgs Singlet Extension of the Standard Model after LHC Run 1*, *Eur. Phys. J. C* **75** (2015) 104, [1501.02234].
- [33] T. Huang, J. M. No, L. Pernié, M. Ramsey-Musolf, A. Safonov, M. Spannowsky et al., *Resonant di-Higgs boson production in the $b\bar{b}WW$ channel: Probing the electroweak phase transition at the LHC*, *Phys. Rev. D* **96** (2017) 035007, [1701.04442].
- [34] C.-Y. Chen, J. Kozaczuk and I. M. Lewis, *Non-resonant Collider Signatures of a Singlet-Driven Electroweak Phase Transition*, *JHEP* **08** (2017) 096, [1704.05844].
- [35] D. Gonçalves, T. Han, F. Kling, T. Plehn and M. Takeuchi, *Higgs boson pair production at future hadron colliders: From kinematics to dynamics*, *Phys. Rev. D* **97** (2018) 113004, [1802.04319].
- [36] A. Alves, T. Ghosh, H.-K. Guo, K. Sinha and D. Vagie, *Collider and Gravitational Wave Complementarity in Exploring the Singlet Extension of the Standard Model*, *JHEP* **04** (2019) 052, [1812.09333].
- [37] A. Alves, T. Ghosh, H.-K. Guo and K. Sinha, *Resonant Di-Higgs Production at Gravitational Wave Benchmarks: A Collider Study using Machine Learning*, *JHEP* **12** (2018) 070, [1808.08974].
- [38] A. Biekötter, D. Gonçalves, T. Plehn, M. Takeuchi and D. Zerwas, *The global Higgs picture at 27 TeV*, *SciPost Phys.* **6** (2019) 024, [1811.08401].
- [39] A. Alves, D. Gonçalves, T. Ghosh, H.-K. Guo and K. Sinha, *Di-Higgs Production in the 4b Channel and Gravitational Wave Complementarity*, *JHEP* **03** (2020) 053, [1909.05268].
- [40] S. Profumo, M. J. Ramsey-Musolf, C. L. Wainwright and P. Winslow, *Singlet-catalyzed electroweak phase transitions and precision Higgs boson studies*, *Phys. Rev. D* **91** (2015) 035018, [1407.5342].

- [41] R. K. Barman, C. Englert, D. Gonçalves and M. Spannowsky, *Di-Higgs resonance searches in weak boson fusion*, *Phys. Rev. D* **102** (2020) 055014, [2007.07295].
- [42] A. Alves, D. Gonçalves, T. Ghosh, H.-K. Guo and K. Sinha, *Di-Higgs Blind Spots in Gravitational Wave Signals*, *Phys. Lett. B* **818** (2021) 136377, [2007.15654].
- [43] D. Gonçalves, A. Kaladharan and Y. Wu, *Electroweak phase transition in the 2HDM: Collider and gravitational wave complementarity*, *Phys. Rev. D* **105** (2022) 095041, [2108.05356].
- [44] D. Gonçalves, A. Kaladharan and Y. Wu, *Resonant top pair searches at the LHC: A window to the electroweak phase transition*, *Phys. Rev. D* **107** (2023) 075040, [2206.08381].
- [45] Anisha, L. Biermann, C. Englert and M. Mühlleitner, *Two Higgs doublets, effective interactions and a strong first-order electroweak phase transition*, *JHEP* **08** (2022) 091, [2204.06966].
- [46] D. Gonçalves, A. Kaladharan and Y. Wu, *Gravitational waves, bubble profile, and baryon asymmetry in the complex 2HDM*, *Phys. Rev. D* **108** (2023) 075010, [2307.03224].
- [47] LISA collaboration, P. Amaro-Seoane et al., *Laser Interferometer Space Antenna*, 1702.00786.
- [48] D. J. H. Chung, A. J. Long and L.-T. Wang, *125 GeV Higgs boson and electroweak phase transition model classes*, *Phys. Rev. D* **87** (2013) 023509, [1209.1819].
- [49] H. H. Patel and M. J. Ramsey-Musolf, *Baryon Washout, Electroweak Phase Transition, and Perturbation Theory*, *JHEP* **07** (2011) 029, [1101.4665].
- [50] C. Wainwright, S. Profumo and M. J. Ramsey-Musolf, *Gravity Waves from a Cosmological Phase Transition: Gauge Artifacts and Daisy Resummations*, *Phys. Rev. D* **84** (2011) 023521, [1104.5487].
- [51] D. Metaxas and E. J. Weinberg, *Gauge independence of the bubble nucleation rate in theories with radiative symmetry breaking*, *Phys. Rev. D* **53** (1996) 836–843, [hep-ph/9507381].
- [52] M. Garny and T. Konstandin, *On the gauge dependence of vacuum transitions at finite temperature*, *JHEP* **07** (2012) 189, [1205.3392].
- [53] C.-W. Chiang, M. J. Ramsey-Musolf and E. Senaha, *Standard Model with a Complex Scalar Singlet: Cosmological Implications and Theoretical Considerations*, *Phys. Rev. D* **97** (2018) 015005, [1707.09960].

[54] S. Arunasalam and M. J. Ramsey-Musolf, *Tunneling potentials for the tunneling action: gauge invariance*, *JHEP* **08** (2022) 138, [2105.07588].

[55] J. Hirvonen, J. Löfgren, M. J. Ramsey-Musolf, P. Schicho and T. V. I. Tenkanen, *Computing the gauge-invariant bubble nucleation rate in finite temperature effective field theory*, *JHEP* **07** (2022) 135, [2112.08912].

[56] J. Löfgren, M. J. Ramsey-Musolf, P. Schicho and T. V. I. Tenkanen, *Nucleation at Finite Temperature: A Gauge-Invariant Perturbative Framework*, *Phys. Rev. Lett.* **130** (2023) 251801, [2112.05472].

[57] K. Kajantie, M. Laine, K. Rummukainen and M. E. Shaposhnikov, *Is there a hot electroweak phase transition at $m_H \gtrsim m_W$?*, *Phys. Rev. Lett.* **77** (1996) 2887–2890, [hep-ph/9605288].

[58] A. D. Linde, *Fate of the False Vacuum at Finite Temperature: Theory and Applications*, *Phys. Lett. B* **100** (1981) 37–40.

[59] S. R. Coleman, *The Fate of the False Vacuum. 1. Semiclassical Theory*, *Phys. Rev. D* **15** (1977) 2929–2936.

[60] C. L. Wainwright, *CosmoTransitions: Computing Cosmological Phase Transition Temperatures and Bubble Profiles with Multiple Fields*, *Comput. Phys. Commun.* **183** (2012) 2006–2013, [1109.4189].

[61] J. M. Moreno, M. Quiros and M. Seco, *Bubbles in the supersymmetric standard model*, *Nucl. Phys. B* **526** (1998) 489–500, [hep-ph/9801272].

[62] P. Athron, C. Balázs and L. Morris, *Supercool subtleties of cosmological phase transitions*, *JCAP* **03** (2023) 006, [2212.07559].

[63] P. Athron, C. Balázs, A. Fowlie, L. Morris and L. Wu, *Cosmological phase transitions: From perturbative particle physics to gravitational waves*, *Prog. Part. Nucl. Phys.* **135** (2024) 104094, [2305.02357].

[64] P. Athron, A. Fowlie, C.-T. Lu, L. Morris, L. Wu, Y. Wu et al., *Can supercooled phase transitions explain the gravitational wave background observed by pulsar timing arrays?*, 2306.17239.

[65] P. Athron, L. Morris and Z. Xu, *How robust are gravitational wave predictions from cosmological phase transitions?*, 2309.05474.

[66] M. S. Turner, E. J. Weinberg and L. M. Widrow, *Bubble nucleation in first-order inflation*

and other cosmological phase transitions, Phys. Rev. D **46** (Sep, 1992) 2384–2403.

[67] P. J. Steinhardt, *Relativistic detonation waves and bubble growth in false vacuum decay, Phys. Rev. D* **25** (Apr, 1982) 2074–2085.

[68] F. Giese, T. Konstandin and J. van de Vis, *Model-independent energy budget of cosmological first-order phase transitions—A sound argument to go beyond the bag model, JCAP* **07** (2020) 057, [2004.06995].

[69] A. H. Guth and S. H. H. Tye, *Phase transitions and magnetic monopole production in the very early universe, Phys. Rev. Lett.* **44** (Mar, 1980) 631–635.

[70] J. Ellis, M. Lewicki and J. M. No, *On the Maximal Strength of a First-Order Electroweak Phase Transition and its Gravitational Wave Signal, JCAP* **04** (2019) 003, [1809.08242].

[71] A. Friedmann, *On the Possibility of a world with constant negative curvature of space, Z. Phys.* **21** (1924) 326–332.

[72] T. Harada, C.-M. Yoo and K. Kohri, *Threshold of primordial black hole formation, Phys. Rev. D* **88** (2013) 084051, [1309.4201].

[73] I. Musco and J. C. Miller, *Primordial black hole formation in the early universe: critical behaviour and self-similarity, Class. Quant. Grav.* **30** (2013) 145009, [1201.2379].

[74] I. Musco, V. De Luca, G. Franciolini and A. Riotto, *Threshold for primordial black holes. II. A simple analytic prescription, Phys. Rev. D* **103** (2021) 063538, [2011.03014].

[75] A. M. Green and B. J. Kavanagh, *Primordial Black Holes as a dark matter candidate, J. Phys. G* **48** (2021) 043001, [2007.10722].

[76] B. Carr, K. Kohri, Y. Sendouda and J. Yokoyama, *Constraints on primordial black holes, Rept. Prog. Phys.* **84** (2021) 116902, [2002.12778].

[77] B. J. Carr, *Pregalactic black hole accretion and the thermal history of the Universe, Monthly Notices of the Royal Astronomical Society* **194** (03, 1981) 639–668, [<https://academic.oup.com/mnras/article-pdf/194/3/639/3214058/mnras194-0639.pdf>].

[78] Y. Ali-Haïmoud and M. Kamionkowski, *Cosmic microwave background limits on accreting primordial black holes, Phys. Rev. D* **95** (2017) 043534, [1612.05644].

[79] K. Griest, A. M. Cieplak and M. J. Lehner, *Experimental Limits on Primordial Black Hole Dark Matter from the First 2 yr of Kepler Data, Astrophys. J.* **786** (2014) 158, [1307.5798].

[80] MACHO collaboration, R. A. Allsman et al., *MACHO project limits on black hole dark matter in the 1-30 solar mass range, Astrophys. J. Lett.* **550** (2001) L169,

[[astro-ph/0011506](#)].

- [81] EROS-2 collaboration, P. Tisserand et al., *Limits on the Macho Content of the Galactic Halo from the EROS-2 Survey of the Magellanic Clouds*, *Astron. Astrophys.* **469** (2007) 387–404, [[astro-ph/0607207](#)].
- [82] D. Croon, D. McKeen, N. Raj and Z. Wang, *Subaru-HSC through a different lens: Microlensing by extended dark matter structures*, *Phys. Rev. D* **102** (2020) 083021, [[2007.12697](#)].
- [83] H. Niikura et al., *Microlensing constraints on primordial black holes with Subaru/HSC Andromeda observations*, *Nature Astron.* **3** (2019) 524–534, [[1701.02151](#)].
- [84] P. Mroz et al., *No massive black holes in the Milky Way halo*, [2403.02386](#).
- [85] P. Mroz et al., *Microlensing optical depth and event rate toward the Large Magellanic Cloud based on 20 years of OGLE observations*, [2403.02398](#).
- [86] W. DeRocco, E. Frangipane, N. Hamer, S. Profumo and N. Smyth, *Revealing terrestrial-mass primordial black holes with the Nancy Grace Roman Space Telescope*, *Phys. Rev. D* **109** (2024) 023013, [[2311.00751](#)].
- [87] K. Griest, A. M. Cieplak and M. J. Lehner, *New limits on primordial black hole dark matter from an analysis of kepler source microlensing data*, *Phys. Rev. Lett.* **111** (Oct, 2013) 181302.
- [88] Z. Yi, Z.-Q. You, Y. Wu, Z.-C. Chen and L. Liu, *Exploring the NANOGrav Signal and Planet-mass Primordial Black Holes through Higgs Inflation*, [2308.14688](#).
- [89] Y. Cai, M. Zhu and Y.-S. Piao, *Primordial black holes from null energy condition violation during inflation*, [2305.10933](#).
- [90] C. Fu and S.-J. Wang, *Primordial black holes and induced gravitational waves from double-pole inflation*, *JCAP* **06** (2023) 012, [[2211.03523](#)].
- [91] M. Solbi and K. Karami, *Primordial black holes formation in the inflationary model with field-dependent kinetic term for quartic and natural potentials*, *Eur. Phys. J. C* **81** (2021) 884, [[2106.02863](#)].
- [92] H. Motohashi, S. Mukohyama and M. Oliosi, *Constant Roll and Primordial Black Holes*, *JCAP* **03** (2020) 002, [[1910.13235](#)].
- [93] C. Fu, P. Wu and H. Yu, *Primordial Black Holes from Inflation with Nonminimal Derivative Coupling*, *Phys. Rev. D* **100** (2019) 063532, [[1907.05042](#)].

[94] S. Ge, J. Guo and J. Liu, *A New Mechanism for Primordial Black Hole Formation from QCD Axion*, 2309.01739.

[95] S. Sugiyama, M. Takada and A. Kusenko, *Possible evidence of axion stars in HSC and OGLE microlensing events*, *Phys. Lett. B* **840** (2023) 137891, [2108.03063].

[96] C. Caprini et al., *Science with the space-based interferometer eLISA. II: Gravitational waves from cosmological phase transitions*, *JCAP* **04** (2016) 001, [1512.06239].

[97] V. Corbin and N. J. Cornish, *Detecting the cosmic gravitational wave background with the big bang observer*, *Class. Quant. Grav.* **23** (2006) 2435–2446, [gr-qc/0512039].

[98] H. Kudoh, A. Taruya, T. Hiramatsu and Y. Himemoto, *Detecting a gravitational-wave background with next-generation space interferometers*, *Phys. Rev. D* **73** (2006) 064006, [gr-qc/0511145].

[99] ATLAS collaboration, *HL-LHC prospects for the measurement of Higgs boson pair production in the $b\bar{b}b\bar{b}$ final state and combination with the $b\bar{b}\gamma\gamma$ and $b\bar{b}\tau^+\tau^-$ final states at the ATLAS experiment*, tech. rep., CERN, Geneva, 2022.

[100] ATLAS collaboration, G. Aad et al., *Combination of searches for resonant Higgs boson pair production using pp collisions at $\sqrt{s} = 13$ TeV with the ATLAS detector*, 2311.15956.

[101] LHC HIGGS CROSS SECTION WORKING GROUP collaboration, D. de Florian et al., *Handbook of LHC Higgs Cross Sections: 4. Deciphering the Nature of the Higgs Sector*, 1610.07922.

[102] “<https://twiki.cern.ch/twiki/bin/view/lhcphysics>.”
<https://twiki.cern.ch/twiki/bin/view/LHCPhysics>.

[103] CMS collaboration, CMS Collaboration, *Search for a new scalar resonance decaying to a pair of Z bosons at the High-Luminosity LHC*, .

[104] ATLAS COLLABORATION collaboration, *HL-LHC prospects for diboson resonance searches and electroweak vector boson scattering in the $WW/WZ \rightarrow \ell\nu qq$ final state*, Tech. Rep. ATL-PHYS-PUB-2018-022, CERN, Geneva, Oct, 2018.

[105] I. M. Lewis and M. Sullivan, *Benchmarks for Double Higgs Production in the Singlet Extended Standard Model at the LHC*, *Phys. Rev. D* **96** (2017) 035037, [1701.08774].

[106] W. Liu and K.-P. Xie, *Probing electroweak phase transition with multi-TeV muon colliders and gravitational waves*, *JHEP* **04** (2021) 015, [2101.10469].

[107] C.-Y. Chen, S. Dawson and I. M. Lewis, *Exploring resonant di-Higgs boson production in*

the Higgs singlet model, Phys. Rev. D **91** (2015) 035015, [1410.5488].

[108] D. Buttazzo, F. Sala and A. Tesi, *Singlet-like Higgs bosons at present and future colliders*, *JHEP* **11** (2015) 158, [1505.05488].

[109] G. Chalons, D. Lopez-Val, T. Robens and T. Stefaniak, *The Higgs singlet extension at LHC Run 2, PoS ICHEP2016* (2016) 1180, [1611.03007].

[110] B. W. Lee, C. Quigg and H. B. Thacker, *Weak interactions at very high energies: The role of the higgs-boson mass*, *Phys. Rev. D* **16** (Sep, 1977) 1519–1531.

[111] P. Bechtle, S. Heinemeyer, T. Klingl, T. Stefaniak, G. Weiglein and J. Wittbrodt, *HiggsSignals-2: Probing new physics with precision Higgs measurements in the LHC 13 TeV era*, *Eur. Phys. J. C* **81** (2021) 145, [2012.09197].

[112] P. Bechtle, S. Heinemeyer, O. Stål, T. Stefaniak and G. Weiglein, *HiggsSignals: Confronting arbitrary Higgs sectors with measurements at the Tevatron and the LHC*, *Eur. Phys. J. C* **74** (2014) 2711, [1305.1933].

[113] H. Bahl, T. Biekötter, S. Heinemeyer, C. Li, S. Paasch, G. Weiglein et al., *HiggsTools: BSM scalar phenomenology with new versions of HiggsBounds and HiggsSignals*, *Comput. Phys. Commun.* **291** (2023) 108803, [2210.09332].

[114] ATLAS collaboration, M. Aaboud et al., *Search for pair production of Higgs bosons in the $b\bar{b}b\bar{b}$ final state using proton–proton collisions at $\sqrt{s} = 13$ TeV with the ATLAS detector*, *Phys. Rev. D* **94** (2016) 052002, [1606.04782].

[115] CMS collaboration, V. Khachatryan et al., *Search for heavy resonances decaying to two Higgs bosons in final states containing four b quarks*, *Eur. Phys. J. C* **76** (2016) 371, [1602.08762].

[116] CMS collaboration, V. Khachatryan et al., *Search for two Higgs bosons in final states containing two photons and two bottom quarks in proton-proton collisions at 8 TeV*, *Phys. Rev. D* **94** (2016) 052012, [1603.06896].

[117] ATLAS collaboration, G. Aad et al., *Searches for Higgs boson pair production in the $hh \rightarrow b\bar{b}\tau\tau, \gamma\gamma WW^*, \gamma\gamma bb, bbbb$ channels with the ATLAS detector*, *Phys. Rev. D* **92** (2015) 092004, [1509.04670].

[118] CMS collaboration, V. Khachatryan et al., *Search for a Higgs boson in the mass range from 145 to 1000 GeV decaying to a pair of W or Z bosons*, *JHEP* **10** (2015) 144, [1504.00936].

[119] CMS collaboration, S. Chatrchyan et al., *Search for a Standard-Model-Like Higgs Boson*

with a Mass in the Range 145 to 1000 GeV at the LHC, *Eur. Phys. J. C* **73** (2013) 2469, [1304.0213].

- [120] ATLAS collaboration, G. Aad et al., *Combination of searches for WW, WZ, and ZZ resonances in pp collisions at $\sqrt{s} = 8$ TeV with the ATLAS detector*, *Phys. Lett. B* **755** (2016) 285–305, [1512.05099].
- [121] ATLAS collaboration, G. Aad et al., *Search for an additional, heavy Higgs boson in the $H \rightarrow ZZ$ decay channel at $\sqrt{s} = 8$ TeV in pp collision data with the ATLAS detector*, *Eur. Phys. J. C* **76** (2016) 45, [1507.05930].
- [122] LHC HIGGS CROSS SECTION WORKING GROUP collaboration, J. R. Andersen et al., *Handbook of LHC Higgs Cross Sections: 3. Higgs Properties*, 1307.1347.
- [123] P. Bechtle, O. Brein, S. Heinemeyer, G. Weiglein and K. E. Williams, *HiggsBounds: Confronting Arbitrary Higgs Sectors with Exclusion Bounds from LEP and the Tevatron*, *Comput. Phys. Commun.* **181** (2010) 138–167, [0811.4169].
- [124] P. Bechtle, O. Brein, S. Heinemeyer, G. Weiglein and K. E. Williams, *HiggsBounds 2.0.0: Confronting Neutral and Charged Higgs Sector Predictions with Exclusion Bounds from LEP and the Tevatron*, *Comput. Phys. Commun.* **182** (2011) 2605–2631, [1102.1898].
- [125] P. Bechtle, O. Brein, S. Heinemeyer, O. Stål, T. Stefaniak, G. Weiglein et al., *HiggsBounds – 4: Improved Tests of Extended Higgs Sectors against Exclusion Bounds from LEP, the Tevatron and the LHC*, *Eur. Phys. J. C* **74** (2014) 2693, [1311.0055].
- [126] P. Bechtle, D. Dercks, S. Heinemeyer, T. Klingl, T. Stefaniak, G. Weiglein et al., *HiggsBounds-5: Testing Higgs Sectors in the LHC 13 TeV Era*, *Eur. Phys. J. C* **80** (2020) 1211, [2006.06007].
- [127] D. López-Val and T. Robens, Δr and the W-boson mass in the singlet extension of the standard model, *Phys. Rev. D* **90** (2014) 114018, [1406.1043].
- [128] M. E. Peskin and T. Takeuchi, *Estimation of oblique electroweak corrections*, *Phys. Rev. D* **46** (Jul, 1992) 381–409.
- [129] K. Hagiwara, S. Matsumoto, D. Haidt and C. S. Kim, *A Novel approach to confront electroweak data and theory*, *Z. Phys. C* **64** (1994) 559–620, [hep-ph/9409380].
- [130] P. D. Group, *Review of Particle Physics, Progress of Theoretical and Experimental Physics* **2022** (08, 2022) 083C01,
[\[https://academic.oup.com/ptep/article-pdf/2022/8/083C01/49175539/ptac097.pdf\]](https://academic.oup.com/ptep/article-pdf/2022/8/083C01/49175539/ptac097.pdf).

- [131] B. W. Lee, C. Quigg and H. B. Thacker, *Weak Interactions at Very High-Energies: The Role of the Higgs Boson Mass*, *Phys. Rev. D* **16** (1977) 1519.
- [132] S. Kanemura and K. Yagyu, *Unitarity bound in the most general two Higgs doublet model*, *Phys. Lett. B* **751** (2015) 289–296, [[1509.06060](#)].
- [133] R.-G. Cai, Z. Cao, Z.-K. Guo, S.-J. Wang and T. Yang, *The Gravitational-Wave Physics*, *Natl. Sci. Rev.* **4** (2017) 687–706, [[1703.00187](#)].
- [134] C. Caprini and D. G. Figueroa, *Cosmological Backgrounds of Gravitational Waves*, *Class. Quant. Grav.* **35** (2018) 163001, [[1801.04268](#)].
- [135] M. Hindmarsh, S. J. Huber, K. Rummukainen and D. J. Weir, *Gravitational waves from the sound of a first order phase transition*, *Phys. Rev. Lett.* **112** (2014) 041301, [[1304.2433](#)].
- [136] M. Hindmarsh, S. J. Huber, K. Rummukainen and D. J. Weir, *Shape of the acoustic gravitational wave power spectrum from a first order phase transition*, *Phys. Rev. D* **96** (2017) 103520, [[1704.05871](#)].
- [137] M. Hindmarsh, *Sound shell model for acoustic gravitational wave production at a first-order phase transition in the early Universe*, *Phys. Rev. Lett.* **120** (2018) 071301, [[1608.04735](#)].
- [138] A. H. Guth and S. H. H. Tye, *Phase transitions and magnetic monopole production in the very early universe*, *Phys. Rev. Lett.* **44** (Apr, 1980) 963–963.
- [139] M. Hindmarsh and M. Hijazi, *Gravitational waves from first order cosmological phase transitions in the Sound Shell Model*, *JCAP* **12** (2019) 062, [[1909.10040](#)].
- [140] H.-K. Guo, K. Sinha, D. Vagie and G. White, *Phase Transitions in an Expanding Universe: Stochastic Gravitational Waves in Standard and Non-Standard Histories*, *JCAP* **01** (2021) 001, [[2007.08537](#)].
- [141] M. B. Hindmarsh, M. Lüben, J. Lumma and M. Pauly, *Phase transitions in the early universe*, *SciPost Phys. Lect. Notes* **24** (2021) 1, [[2008.09136](#)].
- [142] D. Bodeker and G. D. Moore, *Electroweak Bubble Wall Speed Limit*, *JCAP* **05** (2017) 025, [[1703.08215](#)].
- [143] A. Kosowsky, M. S. Turner and R. Watkins, *Gravitational radiation from colliding vacuum bubbles*, *Phys. Rev. D* **45** (1992) 4514–4535.
- [144] A. Kosowsky and M. S. Turner, *Gravitational radiation from colliding vacuum bubbles: envelope approximation to many bubble collisions*, *Phys. Rev. D* **47** (1993) 4372–4391, [[astro-ph/9211004](#)].

- [145] M. Lewicki and V. Vaskonen, *Gravitational waves from bubble collisions and fluid motion in strongly supercooled phase transitions*, *Eur. Phys. J. C* **83** (2023) 109, [[2208.11697](#)].
- [146] M. Kamionkowski, A. Kosowsky and M. S. Turner, *Gravitational radiation from first order phase transitions*, *Phys. Rev. D* **49** (1994) 2837–2851, [[astro-ph/9310044](#)].
- [147] E. Witten, *Cosmic Separation of Phases*, *Phys. Rev. D* **30** (1984) 272–285.
- [148] C. Caprini, R. Durrer and X. Siemens, *Detection of gravitational waves from the QCD phase transition with pulsar timing arrays*, *Phys. Rev. D* **82** (2010) 063511, [[1007.1218](#)].
- [149] C. Caprini, R. Durrer and G. Servant, *The stochastic gravitational wave background from turbulence and magnetic fields generated by a first-order phase transition*, *JCAP* **12** (2009) 024, [[0909.0622](#)].